Preprint of the Published version: Di Nino, S., Mancini, L., Ferretti, M., Di Egidio, A., A reduced-order model for the analysis of underground utility tunnel lifelines protection against transverse seismic excitations. Nonlinear Dyn 114, 256 (2026). https://doi.org/10.1007/s11071-025-12122-y

A Reduced-Order Model for the Analysis of Underground Utility Tunnel Lifelines Protection against Transverse Seismic Excitations

Simona Di Nino · Lorenzo Mancini · Manuel Ferretti · Angelo Di Egidio

Abstract A seismic protection strategy is proposed to mitigate the effects of transverse ground motion on the internal contents of utility tunnels. The approach consists of introducing internal support frames for housing utilities, which are partially decoupled from the tunnel structure through visco-elastic isolators and equipped with vibration control devices. To evaluate the effectiveness of the protection system, a reduced-order analytical model is developed. In this model, the tunnel is idealized as a rigid body embedded in an elastic, compression-only soil medium, and contains an internal rigid frame supporting its contents. This internal frame is decoupled from the tunnel through four visco-elastic devices that connect the utililty tunnel to the internal frame. Additional vibration mitigation is provided by a nonlinear device, consisting of an oscillating mass connected to the internal rigid frame through a hysteretic link and an inerter. This system, referred to as the Hysteretic Mass Damper Inerter (HMDI), enhances energy dissipation and control performance. The proposed low-dimensional model is first validated against a refined Finite Element (FE) benchmark, demonstrating good agreement and confirming its suitability for efficient parametric analyses and preliminary design. The dynamic behavior of the system is then investigated through frequency-domain analyses under harmonic excitation to examine the influence of key control parameters. Finally, time-domain simulations using representative earthquake ground motions are performed to evaluate the system performance under realistic seismic conditions.

Keywords Reduced Order Model · Hysteretic Mass Damper Inerter · Base Isolation · Utility Tunnel · Transverse Seismic Excitation.

1 Introduction

Utility tunnels, also known as service tunnels, are underground passages designed to house and protect essential infrastructure such as water pipes, electrical cables, gas lines, and communication networks [1]. These tunnels allow for centralized and safe access to utilities, facilitating maintenance and reducing the need for disruptive surface excavations. Commonly found in large cities, airports, and industrial complexes, utility tunnels contribute to the efficiency, safety, and resilience of modern urban environments. Accordingly, the development of underground structures has become increasingly widespread in recent years, and it has also become an important direction for urban development.

Although underground tunnels are generally less exposed than above-ground structures, they remain vulnerable to seismic events. Earthquakes can cause significant damage through strong ground shaking, differential ground deformation, and complex soil–structure interaction phenomena [2]. Consequently, extensive research has been conducted on the seismic performance of underground structures, leading to the development of various theories and design methodologies [3,4], as well as mitigation strategies, notably tunnel seismic isolation (e.g., [5]). However, despite its proven effectiveness in reducing seismic response, the broader application of tunnel seismic isolation remains limited due to an incomplete understanding of its governing mechanisms.

In recent years, growing attention has been specifically devoted to the seismic behavior of utility tunnels, as reflected in an increasing number of experimental and numerical studies (e.g., [6,7,8,9,10,11]), some of which also propose seismic isolation strategies to enhance tunnel protection (e.g., [10,11]). Specifically, [10] demonstrates through numerical simulations that the most effective isolation system combines a buffer layer, a cushion, and grouting, strategically arranged between the tunnel and the surrounding soil to attenuate seismic energy transmission. In parallel, [11] shows that the use of tire-derived aggregate as backfill significantly enhances seismic isolation by reducing deformations, bending moments, and shear forces acting on the tunnel lining.

More importantly, in this context, seismic effects can compromise not only the structural integrity of tunnels but also the functionality of the utilities they contain,

S. Di Nino · L. Mancini · M. Ferretti · A. Di Egidio (✉)
Department of Civil, Construction-Architectural and Environmental Engineering, University of L'Aquila, 67100 L'Aquila, Italy
E-mail: angelo.diegidio@univaq.it

underscoring the need for a comprehensive understanding of the seismic response of the entire system. This requires treating the tunnel and its internal utilities as an integrated whole, enabling also the assessment of dynamic behavior of the internal components under seismic loading. To date, only a limited number of studies have addressed this challenge through both experimental investigations and numerical analyses (e.g., [12,13]). For instance, [13] showed that considering the tunnel–pipeline system as an integrated entity reveals a higher seismic vulnerability compared to evaluating its components separately. A few mitigation strategies have also been proposed to reduce seismic effects on the internal components of tunnels (e.g., [14,15]). In particular, [14] investigated the use of seismic isolation devices for pipelines within utility tunnels through shaking table tests and numerical simulations, demonstrating their effectiveness. Similarly, [15] showed that side-wall angle steel supports for utilities significantly enhance their seismic isolation by reducing energy transmission, deformation, and slippage.

In this paper, a seismic protection strategy is proposed to mitigate the effects of transverse ground motion on the internal contents of utility tunnels. The approach involves the introduction of internal support frames housing the utilities, which are partially decoupled from the tunnel structure through visco-elastic isolators. These frames are further equipped with vibration control devices, specifically Hysteretic Mass Damper Inerters (HMDIs). A key contribution of this study lies in the novel application of isolation and control technologies, traditionally employed in building structures (e.g., [16,17,18,19,20,21]), to the investigation of the dynamic behavior of utility tunnels. Particular attention is devoted to the innovative use of HMDIs [22,23], which, together with Tuned Mass Damper Inerters (TMDIs) [24,25,26,27], constitute a new class of hybrid devices with considerable potential for vibration mitigation in Civil Engineering applications. These systems combine the high energy dissipation capacity and robustness to nonlinear behavior of Hysteretic Mass Dampers (HMD) [28,29,30] with the distinctive advantages of inerter-based control devices [31], capable of reproducing the dynamic effects of a large inertial mass without really increasing the system actual weight.

To evaluate the effectiveness of the proposed protection system, extensive parametric analyses are required. Performing such analyses through refined FE models, although highly accurate, is computationally demanding and entails significant processing time. To overcome these limitations, this study introduces an analytical model with a reduced number of degrees of freedom (DOFs), capable of capturing the essential dynamic behavior of the system. In this model, the tunnel is idealized as a rigid body embedded in an elastic, compression-only soil medium. It contains an internal frame, also modeled as a rigid body, that supports the housed equipment. Four discrete visco-elastic devices placed between the tunnel and the internal frame serve to decouple the two components. Additional vibration mitigation is provided by a Hysteretic Mass Damper Inerter (HMDI) connected to the internal frame. The proposed model is first validated against a FE benchmark, demonstrating good agreement and confirming its suitability for rapid parametric studies and preliminary design. Then, the effectiveness of the protection strategy is investigated through frequency-domain parametric analyses under harmonic excitation. Finally, time-domain simulations using a suite of representative earthquake ground motions are performed to assess the system performance under realistic seismic conditions.

The paper is organized as follows. Section 2 describes the low-dimensional mechanical model. Section 3 presents its validation through comparison with a refined FE model for a selected benchmark case. Section 4 defines the key parameters adopted in the parametric analysis. Section 5 discusses the results of the frequency-domain investigation under harmonic excitation, while Sect. 6 addresses the time-domain seismic response analysis. Finally, Sect. 7 summarizes the main findings and outlines directions for future research. Two appendices are provided at the end of the paper.

2 Mechanical low-dimensional model

An underground tunnel system is considered, designed to house various public utility networks, including pipelines, electrical lines, and communication cables. The system is assumed to be subjected to transverse seismic excitation acting in a single direction. The tunnel has a rectangular cross-section with dimensions $2l_x \times 2l_y$ and is embedded in a homogeneous soil medium. Inside the tunnel, supporting frames are installed at regular intervals l_z to carry the utility lines. Each frame has a rectangular shape with dimensions $2l_x^* \times 2l_y^*$. The total mass of the tunnel and its contents acting on each interval l_z is denoted by m_1 and m_c, respectively, while each frame has a mass m_2. The internal frame is partially isolated from the tunnel structure by means of isolation devices, which allow relative motion along the seismic direction[1] and provide energy dissipation during seismic events. Additionally, to further restrict the movement

[1] The direction of relative motion coincides with the seismic direction only under infinitesimal kinematic assumptions, which are considered valid here.

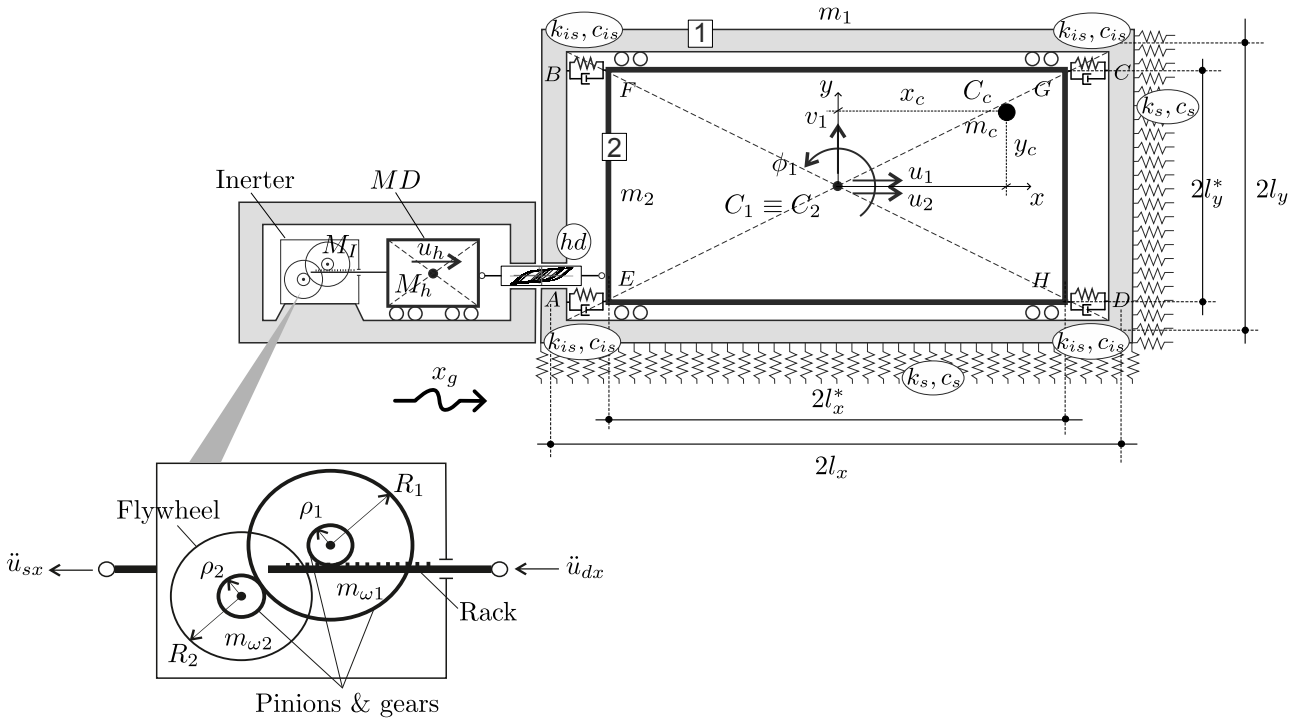

Fig. 1 Mechanical model representation in the tunnel cross-section plane.

of the internal frame, a passive control device, installed within a manhole integrated into the tunnel structure, is connected to the frame. The connection is designed to be active only along the seismic direction, and does not exert any significant influence on the other kinematic degrees of freedom.

For this system, a low-dimensional mechanical model is developed to analyze the dynamic response in the cross-section plane under transverse seismic excitation acting in the horizontal direction (Fig. 1). The model comprises two rigid bodies, the tunnel (Body 1 of mass m_1) and the internal frame (Body 2 of mass m_2), which are internally constrained to allow only relative motion along the horizontal axis. This by four discrete elements, obeying to a linear visco-elastic constitutive law and positioned at the corners of the internal frame. The internal contents are represented by an equivalent lumped mass m_c, rigidly attached to Body 2. The surrounding soil is modeled as a visco-elastic Winkler-type foundation with no tensile resistance. Additionally, a point mass M_h, connected on one side to an inerter and on the other side to a corner of the internal frame via a discrete hysteretic element acting in the horizontal direction, forming a HMDI, is considered and modeled for vibration mitigation. The entire mechanical system is subjected to a prescribed ground displacement in the horizontal direction, $x_G = x_G(t)$.

2.1 Kinematics

The kinematics of the model is described by: (i) The in-plane displacement fields of the rigid Bodies 1 and 2; (ii) The horizontal displacement of HMDI device. In what follows, the assumption of infinitesimal kinematics is adopted, i.e., small displacements and small rotations.

With reference to a Cartesian coordinate system $O(x, y)$, represented in Fig. 1, u_j, v_j, ϕ_j $(j = 1, 2)$ are referred to *generalized displacements*, namely, the time-dependent horizontal and vertical translations u_j, v_j, and the rotation ϕ_j about the z-axis, orthogonal to the (x, y) plane and passing through point O. Under suitable constraint conditions, specifically that Body 2 is only allowed to move horizontally with respect to Body 1, and thus cannot undergo independent vertical translation or rotation, the following kinematic constraints hold: $v_2 = v_1$ and $\phi_2 = \phi_1$. Accordingly, the system kinematics is described by four generalized displacements, that are the translations (u_1, v_1) and rotation (ϕ_1) of the Body 1 (i.e., the tunnel) and the horizontal translation (u_2) of the Body 2 (i.e., the internal frame). To these, a fifth kinematic parameter is added, describing the horizontal displacement u_h of the point mass M_h of the HMDI. Therefore, the proposed mechanical model is low-dimensional, with 5 DOFs, also referred to as Lagrangian parameters, collected in the vector $\mathbf{q} = \left(u_1\ v_1\ \phi_1\ u_2\ u_h\right)^T$.

For later purposes, it is useful to express the displacements to the masses of the system, namely: u_{m_1}, v_{m_1} and u_{m_2}, v_{m_2} of the masses m_1 and m_2, located at the centers of mass C_1 and C_2, respectively, with $C_1 \equiv C_2 \equiv O$; u_{m_c}, v_{m_c} of the total mass of the content m_c, occupying the in-plane position $C_c = (x_c, y_c)$; u_M of the mass M_h of the HMDI. Considering that the system is subjected to the ground displacement in the horizontal direction, $x_G = x_G(t)$, they read:

$$\begin{aligned} u_{m_1} &= u_1 + x_G, & v_{m_1} &= v_1, \\ u_{m_2} &= u_2 + x_G, & v_{m_2} &= v_1, \\ u_{m_c} &= u_2 - \phi_1 y_c + x_G, & v_{m_c} &= v_1 + \phi_1 x_c, \\ u_M &= u_h + x_G, \end{aligned} \tag{1}$$

where the time dependence is omitted for brevity.

2.2 Visco-elastic isolation devices

The isolation devices are modeled as four discrete visco-elastic elements, each connecting a corner of Body 2 (the internal frame) to Body 1 (the tunnel), as illustrated in Fig. 1. The configuration of each element is uniquely defined by the positions of its two endpoints, P_i and P_j, with the horizontal relative displacement expressed as $\Delta = u_{P_j} - u_{P_i}$. Thus, for the devices positioned on the right side of the internal frame, $\Delta = \Delta^+ = u_1 - u_2$; conversely, for the devices located on the left side, $\Delta = \Delta^- = u_2 - u_1$.

According to a Kelvin–Voigt model, the constitutive law governing the force transmitted by each element is given by:

$$F_{is} = k_{is}\Delta + c_{is}\dot{\Delta}, \tag{2}$$

where k_{is} and c_{is} represent the elastic stiffness and viscous damping coefficients, respectively, with the dot denoting time differentiation.

2.3 Hysteretic Mass Damper Inerter device

The HMDI is a vibration control device that integrates two key mechanical components: a mass damper (MD) equipped with a hysteretic (H) energy dissipation mechanism, and an inerter (I).

2.3.1 Hysteretic Mass Damper

The Hysteretic Mass Damper (HMD) is modeled as a point mass M_h connected to the bottom-left corner of the internal frame (of in-plane coordinates $(-l_x^*, -l_y^*)$), through a discrete hysteretic element, which introduces a nonlinear restoring force F_h into the system. Letting $\Delta_h = \left(u_2 + \phi_1 l_y^*\right) - u_h$ the relative horizontal displacement of HMD with respect to the internal frame, the restoring force generated follows the Bouc–Wen model (originally introduced by [32,33] and later extended by [34]) according to the law:

$$F_h = \psi k_h \Delta_h + k_h u_y \left(1 - \psi\right) z_h + c_h \dot{\Delta}_h, \tag{3}$$

Here, k_h is the initial elastic stiffness, c_h a linear damping coefficient, $\psi \in [0, 1]$ is the ratio between the post-yielding and the initial elastic stiffnesses, u_y denotes the yield displacement, and z_h is the dimensionless, non-observable hysteretic variable that evolves according to the following nonlinear differential equation [35,36]:

$$\dot{z}_h = \frac{\dot{\Delta}_h}{u_y}\left[A_h - |z_h|^n \left(\beta + \gamma \,\mathrm{sign}\left(\dot{\Delta}_h\, z_h\right)\right)\right]. \tag{4}$$

In the latter, sign denotes the signum function, and A_h, β and $\gamma > 0$ are dimensionless parameters that govern the behavior of the hysteresis model. In particular, for $\psi = 0$, the parameters β and γ control the shape and size of the hysteresis loop, respectively. The model exhibits a softening hysteretic response when $\beta > 0$, and a hardening response when $\beta < 0$. Moreover, larger values of γ result in broader hysteresis loops, corresponding to increased energy dissipation. The exponential parameter n governs the abruptness of the transition between the elastic and post-elastic branches of the hysteresis model. For large values of n, the Bouc–Wen model behaves similarly to a bilinear model. All simulations presented in this paper are carried out assuming $n = 1$. When $\psi = 0$ and $c_h = 0$, as assumed throughout the paper except for the latter in Sect. 3, and knowing that $F_y = k_h u_y$, the hysteretic cycles depend only on the ratios F_h/F_y and Δ_h/u_y (see Eqs. 3 and 4). Figure 2 shows the dependence of the hysteretic cycles on the parameters β and γ.

2.3.2 Inerter

The mechanical inerter configuration considered in this work, commonly adopted in seismic applications, is of the rack-and-pinion-flywheel type, which converts relative translational motion between its terminals into rotational motion. This transformation is achieved through a mechanical linkage, typically a screw or rack-and-pinion mechanism, that transmits the relative displacement to a rotating flywheel. In this paper, a simplified configuration with two flywheels is adopted, as illustrated in Fig. 1. As the terminals move relative to each other, the linkage induces rotation in the flywheels, generating a reaction force F_I proportional to the relative acceleration, according to the following relation [37]:

$$F_I = M_I(\ddot{u}_{dx} - \ddot{u}_{sx}), \tag{5}$$

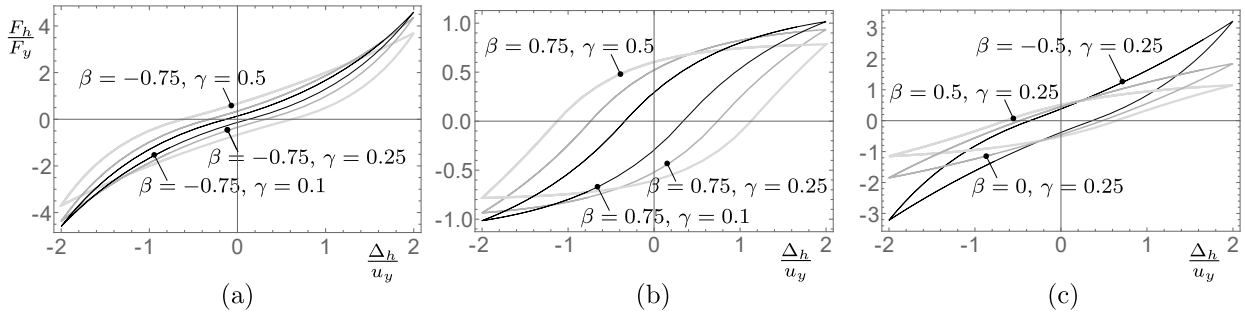

Fig. 2 Hysteresis curves of Bouc-Wen model. Role of parameters: (a) γ in hardening behavior ($\beta = -0.75$); (b) γ in softening behavior ($\beta = 0.75$); (c) β ($\gamma = 0.25$). The displacement is set $\triangle_h = 2u_y \sin(t)$, $u_y = 0.1$ m.

Here, M_I is the inertance (or virtual mass), which is a constant with units of mass, derived from the rotational inertia of the flywheels; for a general multistage mechanism involving N flywheels, the inertance is given by:

$$M_I = \frac{1}{2} m_{\omega 1} \frac{R_1^2}{\rho_1^2} + \frac{1}{2} m_{\omega 2} \frac{R_1^2 R_2^2}{\rho_1^2 \rho_2^2} + \cdots + \frac{1}{2} m_{\omega i} \frac{R_1^2 R_2^2 \cdots R_i^2}{\rho_1^2 \rho_2^2 \cdots \rho_i^2} + \cdots + \frac{1}{2} m_{\omega N} \frac{R_1^2 R_2^2 \cdots R_N^2}{\rho_1^2 \rho_2^2 \cdots \rho_N^2}, \tag{6}$$

where R_i and ρ_i are the external and internal radii, respectively, and $m_{\omega i}$ is the mass of the i-th flywheel.

In this study, since only two flywheels are considered ($N = 2$), and assuming that the left terminal is directly connected to the ground, so that $\ddot{u}_{sx} = \ddot{x}_G$, while the right terminal is connected to the HMD, so that $\ddot{u}_{dx} = \ddot{x}_G + \ddot{u}_h$, the inertial restoring force simplifies to:

$$F_I = M_I \, \ddot{u}_h, \tag{7}$$

where:

$$M_I = \frac{1}{2} m_{\omega 1} \frac{R_1^2}{\rho_1^2} + \frac{1}{2} m_{\omega 2} \frac{R_1^2 R_2^2}{\rho_1^2 \rho_2^2}. \tag{8}$$

2.4 Visco-elastic soil model

A Winkler-type foundation is adopted to model the soil medium, which is assumed to have no tensile strength. That is, the soil responds elastically under compressive loads but offers no resistance to tension. Consequently, the soil reaction to the displacement field of Body 1 is illustrated in Fig. 3, which shows the stress distribution along each side of the tunnel. This distribution arises from the well-known laws of small displacements and rotations for a rigid body, leading to the superposition of two translational displacement components and one rotational component. In the figure, gray regions denote zones under compression, while white regions indicate areas where the foundation is disengaged due to the lack of tensile resistance.

As illustrated in Fig. 3, compression on one side of the tunnel corresponds to tension on the opposite side, and vice versa. Consequently, the soil behaves overall as fully reactive, and the resulting stress distribution is equivalent to that produced by a Winkler foundation capable of resisting both compressive and tensile forces, acting along two sides of the tunnel, namely one horizontal and one vertical side. This observation allows for a significant simplification of the mechanical model, in which the foundation is idealized as a linear Winkler-type system acting only along the boundaries at $x = l_x$ and $y = -l_y$, as shown in Fig. 1.

To incorporate the time-dependent (viscous) behavior of the soil, the Kelvin-Voigt constitutive law is used for the proposed linear Winkler model [38]. Accordingly, the distributed forces $p_x(y)$ and $p_y(x)$ exerted by the soil follow the law:

$$\begin{aligned} p_x(y) &= k_s \Delta_{sx} + c_s \dot{\Delta}_{sx}, \\ p_y(x) &= k_s \Delta_{sy} + c_s \dot{\Delta}_{sy}, \end{aligned} \tag{9}$$

with $\Delta_{sx} = \phi_1 y - u_1$ and $\Delta_{sy} = v_1 + \phi_1 x$. Here, k_s and c_s denote elastic stiffness and viscous damping coefficient, respectively. The soil stiffness is obtained by multiplying the subgrade reaction modulus K by the spacing between the internal frames l_z, resulting in $k_s = K\, l_z$. The damping coefficient, on the other hand, is derived from a prescribed damping ratio ζ_s, associated with an equivalent single-degree-of-freedom (SDOF) oscillator in the horizontal direction. This equivalent system has a total mass of $m_1 + m_2 + m_c$, a stiffness of $2k_s l_y$, and a damping coefficient of $2c_s l_y$. Accordingly, the damping coefficient is given by:

$$c_s = \zeta_s \sqrt{\frac{2\, K\, l_z\, (m_1 + m_2 + m_c)}{l_y}}. \tag{10}$$

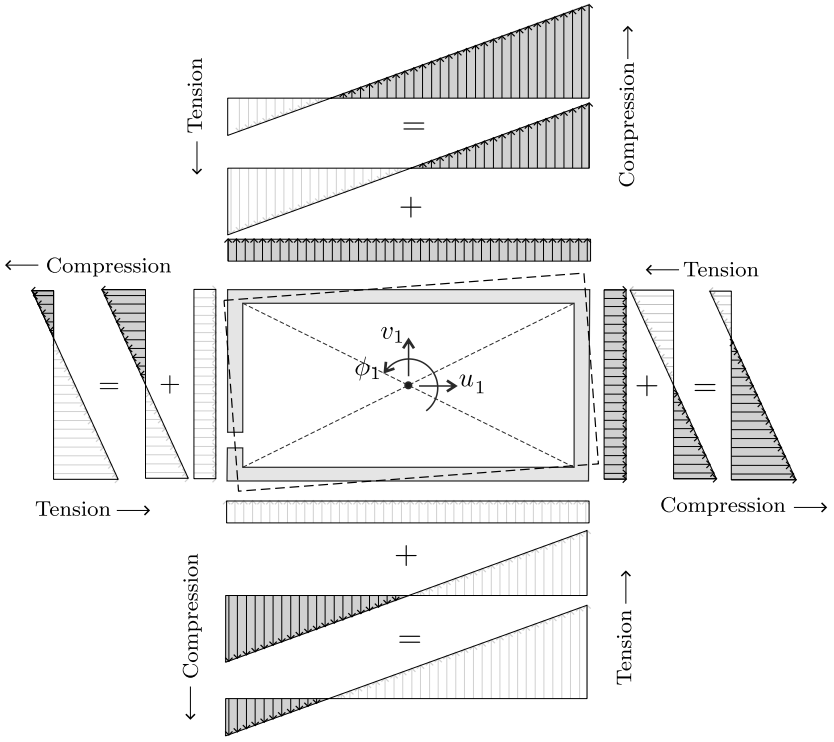

Fig. 3 Soil stress field induced by tunnel kinematics.

2.5 Lagrangian equations of motion

The equations of motion are derived using the Lagrangian formulation, which involves defining the kinetic energy T, potential energy V, and the virtual work δW associated with non-conservative forces.

The kinetic and potential energies, expressed in terms of displacements of the centers of mass, as defined in Sect. 2.1, are given by:

$$T = \frac{1}{2}m_1\left(\dot{u}_{m_1}^2 + \dot{v}_{m_1}^2\right) + \frac{1}{2}J_1\dot{\phi_1}^2 + \frac{1}{2}m_2\left(\dot{u}_{m_2}^2 + \dot{v}_{m_2}^2\right) + \frac{1}{2}J_2\dot{\phi_1}^2 + \frac{1}{2}m_c\left(\dot{u}_{m_c}^2 + \dot{v}_{m_c}^2\right) + \frac{1}{2}M_h\dot{u}_M^2 + \frac{1}{2}M_I\dot{u}_h^2, \tag{11}$$

where J_1 and J_2 are the moment of inertia of the tunnel (Body 1) and the internal frame (Body 2), respectively, about the z-axis, and:

$$V = \left(m_1 v_{m_1} + m_2 v_{m_2} + m_c v_{m_c}\right) g, \tag{12}$$

with g the gravitational acceleration.

Accordingly, the Lagrangian is $L = T - V$.

The virtual work of non-conservative forces, arising from the visco-elastic isolation devices (δW_{is}), the HMD control device (δW_h) and the visco-elastic soil (δW_s), is expressed as:

$$\delta W = \delta W_{is} + \delta W_h + \delta W_s, \tag{13}$$

with:

$$\begin{aligned}
\delta W_{is} &= -2\left(F_{is}^{+}\delta\Delta^{+} + F_{is}^{-}\delta\Delta^{-}\right),\\
\delta W_h &= -F_h\delta\Delta_h,\\
\delta W_s &= -\int_{-l_y}^{l_y} p_x(y)\,\delta\Delta_{sx}\,\mathrm{d}y - \int_{-l_x}^{l_x} p_y(x)\,\delta\Delta_{sy}\,\mathrm{d}x.
\end{aligned} \tag{14}$$

Here, $F_{is}^{\pm}$ denotes the force F_{is} from Eq. 2, evaluated at $\Delta = \Delta^{\pm}$, with $\Delta^{\pm}$ defined in Sect. 2.2.

By expressing the virtual work as $\delta W = \mathbf{Q}^T\delta\mathbf{q}$, the equations of motion are obtained from Lagrange equations:

$$\frac{\mathrm{d}}{\mathrm{d}t}\left(\frac{\partial L}{\partial\dot{\mathbf{q}}}\right) - \frac{\partial L}{\partial\mathbf{q}} = \mathbf{Q}, \tag{15}$$

where $\mathbf{q}$ is the vector of generalized coordinates (defined in Sect. 2.1) and $\mathbf{Q}$ is the vector of the corresponding generalized forces. Using the definitions introduced above, and referring to A for detailed derivations, the

resulting equations of motion can be written as:

$$\begin{aligned}
&m_1\ddot{u}_1 + 4k_{is}\left(u_1 - u_2\right) + 4c_{is}\left(\dot{u}_1 - \dot{u}_2\right) \\
&+ 2k_s l_y u_1 + 2c_s l_y \dot{u}_1 = -m_1\ddot{x}_G, \\
&\left(m_1 + m_2 + m_c\right)\ddot{v}_1 + m_c x_c \ddot{\phi}_1 + 2k_s l_x v_1 \\
&+ 2c_s l_x \dot{v}_1 = -\left(m_1 + m_2 + m_c\right) g, \\
&\left[J_1 + J_2 + m_c\left(x_c^2 + y_c^2\right)\right]\ddot{\phi}_1 + m_c\left(x_c\ddot{v}_1 - y_c\ddot{u}_2\right) \\
&+ \frac{2}{3}k_s\left(l_x^3 + l_y^3\right)\phi_1 + \frac{2}{3}c_s\left(l_x^3 + l_y^3\right)\dot{\phi}_1 \\
&+ F_h l_y^* = m_c y_c \ddot{x}_G - m_c x_c g, \\
&\left(m_2 + m_c\right)\ddot{u}_2 - m_c y_c \ddot{\phi}_1 + 4k_{is}\left(u_2 - u_1\right) \\
&+ 4c_{is}\left(\dot{u}_2 - \dot{u}_1\right) + F_h = -\left(m_c + m_2\right)\ddot{x}_G, \\
&\left(M_h + M_I\right)\ddot{u}_h - F_h = -M_h\ddot{x}_G,
\end{aligned} \tag{16}$$

where F_h is defined in Eq. 3, with z_h given by Eq. 4, and $\Delta_h = (u_2 + \phi_1 l_y^*) - u_h$.

2.6 Calibration of the isolation and control parameters

The stiffness and damping parameters of the isolation and control devices are separately calibrated to match the target period and damping ratio of equivalent SDOF visco-elastic oscillators, as illustrated below.

In particular, the parameters related to the isolation elements are defined as functions of a target isolation period T_{is} and a fixed damping ratio ζ_{is}, corresponding to an equivalent SDOF oscillator in the horizontal direction. This equivalent system is characterized by a total mass $m_2 + m_c$, an effective stiffness $4k_{is}$, and an effective damping $4c_{is}$. Accordingly, the stiffness and damping coefficients of the isolation devices are derived from the following expressions:

$$\begin{aligned}
k_{is} &= \pi^2 \frac{m_2 + m_c}{T_{is}^2}, \\
c_{is} &= \pi \frac{m_2 + m_c}{T_{is}} \zeta_{is}.
\end{aligned} \tag{17}$$

Similar considerations apply to the HMDI, whose total mass is given by:

$$M := M_h + M_I, \tag{18}$$

where M_I is the inertance and M_h is the mass of the hysteretic mass damper. Accordingly, the elastic stiffness k_h and the linear damping c_h of the HMDI are calibrated based on a target period T_h and a fixed damping ratio ζ_h, defined with respect to an equivalent SDOF oscillator in the horizontal direction. The resulting expressions for the stiffness and damping are given as follows:

$$\begin{aligned}
k_h &= 4\pi^2 \frac{M}{T_h^2}, \\
c_h &= 4\pi \frac{M}{T_h} \zeta_h.
\end{aligned} \tag{19}$$

For practical purposes, both M_h and M_I can be conveniently expressed as fractions of the mass $m_2 + m_c$, using the dimensionless coefficients η_h and η_I, respectively:

$$M_h = \eta_h (m_2 + m_c), \tag{20}$$

and:

$$M_I = \eta_I (m_2 + m_c). \tag{21}$$

It is worth noting that, when the inerter is not included in the control system (i.e., $\eta_I = 0$), the stiffness k_h depends solely on the actual mass M_h.

3 Finite element analysis and model validation

The accuracy of the proposed analytical model is assessed through comparisons with FE analyses, carried out on a water pipeline running inside a utility tunnel. Comparisons are made on a specific arrangement, indicated as benchmark case study.

3.1 Benchmark case study

The benchmark case study involves a 60-meter-long water pipeline installed within a utility tunnel characterized by a rectangular cross-section, as in [7]. The tunnel extends 3 m beyond both ends of the pipeline and is embedded in homogeneous soil, classified as “gravel with sand” (sandy gravel). The tunnel is constructed using C60 concrete, in compliance with the Chinese GB standards [39]. The pipeline features a DN400 cross-section, corresponding to an external radius of 213 mm, and is manufactured from a custom-defined steel with a mass density of 7′846 kg/m^3. Its spatial position is defined with reference to its center of mass, which is located at an eccentric point C_{c1} with respect to the geometric centroid of the tunnel cross-section. The pipeline is rigidly anchored to internal support frames placed at regular intervals of 6 m. These frames are made of the same steel material as the pipeline and are composed of HEB300 profiles [40]. A schematic representation of the in-plane benchmark configuration is provided in Fig. 4.

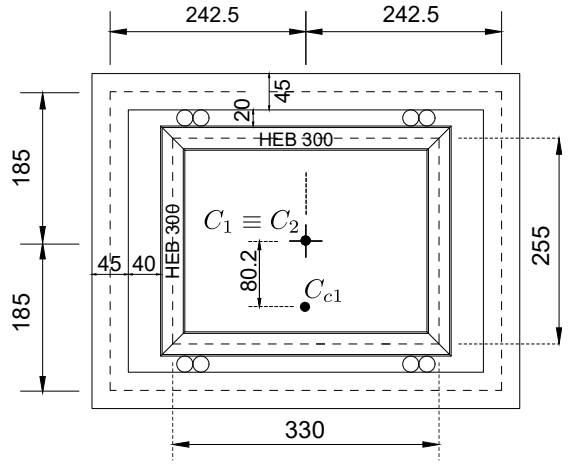

Fig. 4 In-plane geometric characteristics of the benchmark case study; unit of measurement in centimeters.

Accordingly, the geometric and mechanical properties, as well as the masses of the low-dimensional mechanical model described in Sect. 2, are summarized in Table 1. In this table, the mass of the content (m_c) also accounts for the presence of water in the pipeline, considering that it is pressurized, so that the water acts as a uniformly distributed line mass. Moreover, the stiffness of the soil is estimated according a subgrade reaction modulus of about $K = 166'667$ kN/m^3, selected based on the soil type [41,42], while the damping is evaluated according to Eq. 10 with $\zeta_s = 0.1$.

Utility Tunnel	$m_1 = 117'660.6$ kg, $l_z = 6$ m, $l_x = 2.425$ m, $l_y = 1.85$ m, $J_1 = 724'715.5$ kg m^2
Internal Frame	$m_2 = 1'368.78$ kg, $l_x^* = 1.65$ m, $l_y^* = 1.275$ m, $J_2 = 3'903.6$ kg m^2
Content	$m_{c1} = 1'407.08$ kg, $C_{c1} = (0, -0.802)$ m
Soil	$k_s = 1'000'000$ kN/m^2, $c_s = 1'141'412.73$ kg/s m

Table 1 Geometric, mass, and mechanical characteristics of the analytical model.

An isolation and control system is included to partially decouple each internal frame from the tunnel structure, thereby allowing relative motion exclusively in the horizontal direction. In addition, a Tuned Mass Damper (TMD), with a mass equal to 10 % of the combined mass of the frame and its contents, is connected to each frame to further mitigate horizontal relative vibrations between the internal frames and the pipeline.

The isolation and control parameters of the analytical model are calibrated following the Sect. 2.6. Specifically, for the visco-elastic isolation elements, the target isolation period $T_{is} = 2$ s and the damping ratio $\zeta_{is} = 0.1$ are fixed. Regarding HMDI, it is initially simplified to a TMD configuration by setting the constitutive parameter $\psi = 1$ in Eq. 3 and assuming $\eta_I = 0$. Then, the parameters $\eta_h = 0.1$, $T_h = 2$ s and $\zeta_h = 0.1$ are fixed. The resulting stiffness and damping coefficients are summarized in Table 2.

Isolation devices	$k_{is} = 6.849$ kN/m, $c_{is} = 436.031$ kg/s
TMD	$k_h = 2.74$ kN/m, $c_h = 174.412$ kg/s, $\psi = 1$, $\eta_I = 0$ ($M_I = 0$), $\eta_h = 0.1$ ($M_h = 277.586$ kg)

Table 2 Isolation and control parameters of the analytical model.

3.2 FE model

A FE model of the benchmark case study is developed and analyzed using the commercial software SAP2000 (Fig. 5).

The tunnel walls are modeled using thick shell elements, which follow an isotropic linear constitutive law. The corresponding elastic modulus and Poisson ratio are 36 GPa and 0.2, respectively, while the mass density is $2'548$ kg/m^3. The wall geometry is discretized using a structured rectangular mesh.

The internal frame structures are modeled using beam elements governed by isotropic linear laws, with elastic modulus and Poisson ratio 210 GPa and 0.3, respectively; the mass density is $7'846$ kg/m^3. Also the pipeline is modeled using beam elements, having the centroid at the height of the center of mass C_{c1}. It is rigidly connected to the frame structures and is assumed to be made of the same material; an additional linear mass of 132 kg/m is assigned to the beam to account for the mass of the pressurized water it conveys.

The surrounding soil is modeled using visco-elastic link elements connected to the surfaces of the two orthogonal walls of the tunnel, as detailed in Sect. 2.4. The stiffness and damping coefficients of these elements are derived by dividing the corresponding values from the analytical model (reported in Table 1) with respect to the spacing between adjacent internal frames, namely, $166'667$ kN/m^3 (i.e., the subgrade reaction modulus) and $190'235$ kg/s m^2, respectively.

Each internal frame is partially isolated from the tunnel by means of internal constraints that permit only relative horizontal motion. This relative motion is governed by four two-node visco-elastic link elements, which connect the corners of the internal frames to the tunnel walls. These elements are assigned the same stiffness and damping coefficients as those used in the analytical

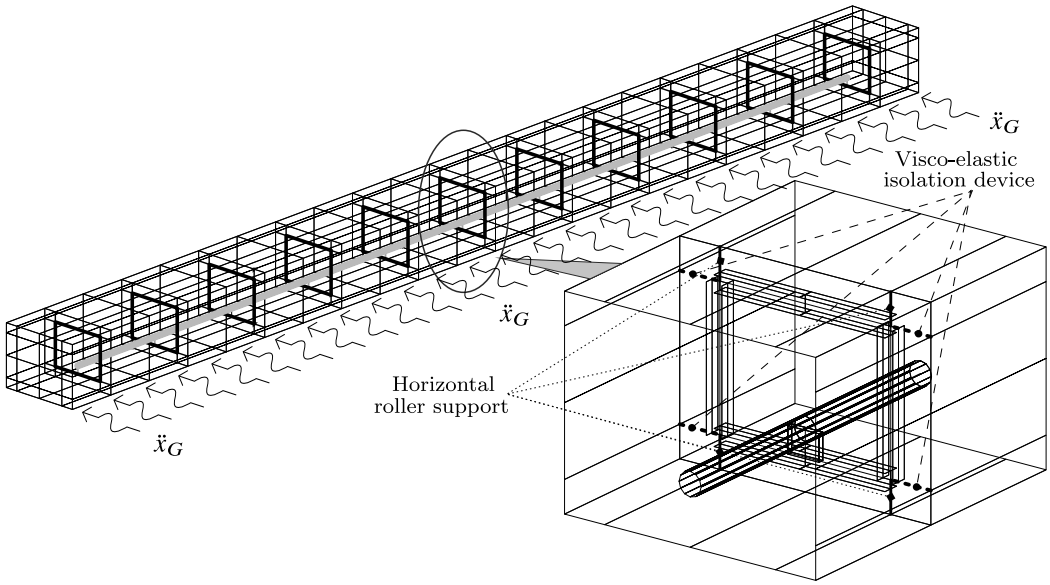

Fig. 5 Finite Element Model of the benchmark case study.

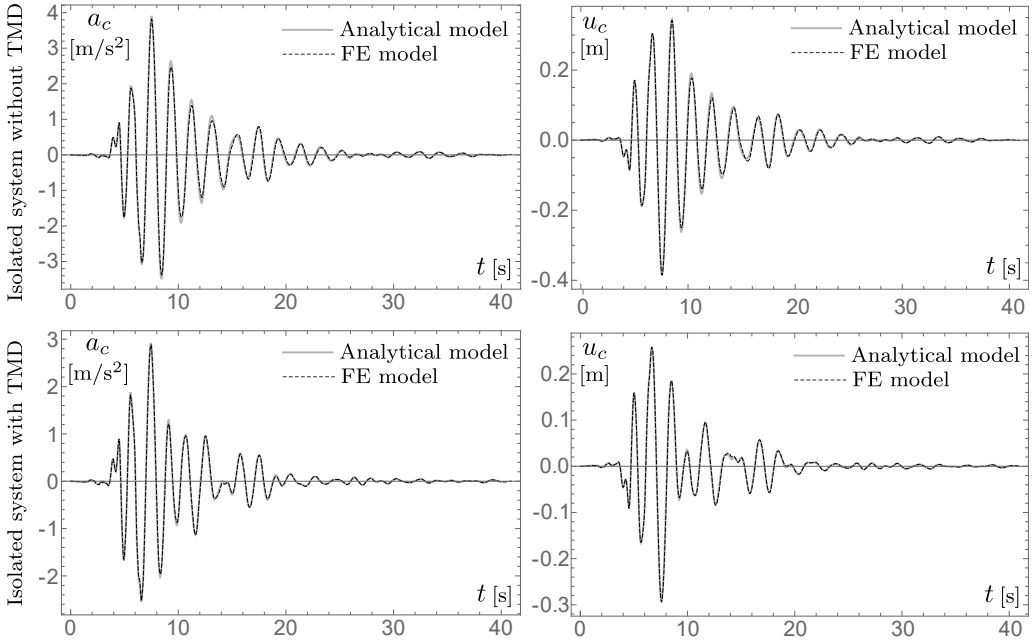

Fig. 6 Benchmark case study: time-histories of content acceleration and displacement. Comparison between the FE model (dashed line) and the analytical model (solid gray line).

model, as reported in Table 2 (i.e., 6.849 kN/m and 436.031 kg/s, respectively). Additionally, point masses of 277.586 kg are connected to one corner of each internal frame through visco-elastic links to represent the TMD. These links are also assigned the same mechanical properties as in the analytical model, specifically, a stiffness of 2.74 kN/m and a damping coefficient of 174.412 kg/s, respectively, as reported in Table 2.

In total, the FE model includes 11 point masses, 87 beam elements, 384 shell elements, corresponding to a total of 2800 DOFs.

3.3 Numerical results

Structural analyses are performed to evaluate the seismic response of the isolated utility tunnel defined in the benchmark case study. The system is subjected to horizontal transverse ground motion (x_G) derived from the Kobe earthquake record. Details of the seismic input are provided in Sect. 6.1, along with Fig. 11.

Numerical analyses are conducted on both the analytical and FE models, considering two scenarios: the uncontrolled configuration (without the TMD) and the

controlled configuration (with the TMD). The results are compared in terms of the time-histories of the horizontal acceleration and displacement of the content, denoted as a_c and u_c, respectively, as shown in Fig. 6. A very good agreement is observed between the analytical and FE results in both scenarios, thereby validating the analytical formulation.

4 Definition of Analysis Parameters

An extensive parametric analysis is carried out to evaluate the effectiveness of the protection system with respect to selected system parameters. The system is deemed effective if it leads to a reduction in the absolute acceleration of the content (a_c) compared to the unprotected configuration, while simultaneously limiting the horizontal displacement of the internal frame (u_2).

In the following, a distinction is made between the parameters that will be varied in the analysis and those that will be held constant.

4.1 Variable parameters

The varying parameters are listed below.

Isolation parameters

- The target period T_{is} of the isolation devices, and, as a consequence, their stiffness and damping characteristics as defined by Eq. 17.

Control parameters

- The total mass M of the HMDI, defined through the mass coefficients η_h and η_I (Eq. 18), associated with the hysteretic mass damper and the inerter, respectively, as given by Eq. 20 and Eq. 21.
- The target period T_h of the HMDI, and, as a consequence, its linear stiffness and damping characteristics as defined by Eq. 19.
- The coefficient β and yield displacement u_y of the hysteretic law governing the HMDI, as defined by Eq. 4; in particular, values of β that capture both hardening and softening behaviors of the device are investigated.

Content

- The total mass, m_c, and the position of the mass center, $C_c = (x_c, y_c)$, of the content. In particular, two distinct cases are studied: (i) $m_{c1} = 1'407.08$ kg and $C_{c1} = (0, -0.802)$ m, (as in the benchmark case), and (ii) $m_{c2} = 3\, m_{c1} = 4'221.24$ kg and $C_{c2} = (1, -0.802)$ m.

4.2 Fixed parameters

The parameters considered fixed, as their variability is deemed not relevant for the purposes of this study, are listed below.

Tunnel and internal frames

- The geometrical and mechanical properties of the tunnel and the internal frame, as detailed in Table 1.

Soil

- The mechanical properties of the soil, as detailed in Table 1, except in the analysis of Sect. 5.1.

Isolation and control parameters

- The target damping ratio of the isolation devices, $\zeta_{is} = 0.1$, and the target damping ratio associated with the linear part of the HMDI, $\zeta_h = 0$ (from which $c_h = 0$). This latter value is related to the decision to rely solely on the nonlinear hysteretic behavior of the HMDI device for its energy dissipation capacity.
- The following constitutive parameters of the HMDI: $\psi = 0$, $A_h = 1$ and $\gamma = 0.25$; the latter accounts for dissipation capability of the device.

5 Harmonic excitation

The first set of analyses considers a harmonic base acceleration with ground acceleration given by:

$$\ddot{x}_G(t) = a \sin(\Omega\, t) \tag{22}$$

where a denotes the amplitude of the excitation and Ω its circular frequency. Accordingly, the period of the harmonic excitation is given by $T_\Omega = \frac{2\pi}{\Omega}$. The results are presented in two types of frequency-response curves: one showing the maximum acceleration a_c of the center of mass of the content, and the other illustrating the maximum horizontal displacement u_2 of the internal frame. Both curves are plotted as functions of the excitation frequency Ω. All frequency-response curves in this section are obtained for a fixed excitation amplitude of $a = 0.1g\,\mathrm{m/s^2}$.

5.1 Independence of the response of the isolated system from the soil characteristics

The first analysis aims to assess the influence of soil properties on the response of the utility tunnel with the seismically isolated internal frame. To this end, frequency-response curves are generated for two configurations: the unprotected utility tunnel and the tunnel equipped solely with the isolated internal frame, without any HMD or HMDI. The analysis is carried out for three different values of soil stiffness k_s. The results related to the system without seismic isolation of the internal frame are obtained by numerically solving the equations of motion presented in B.

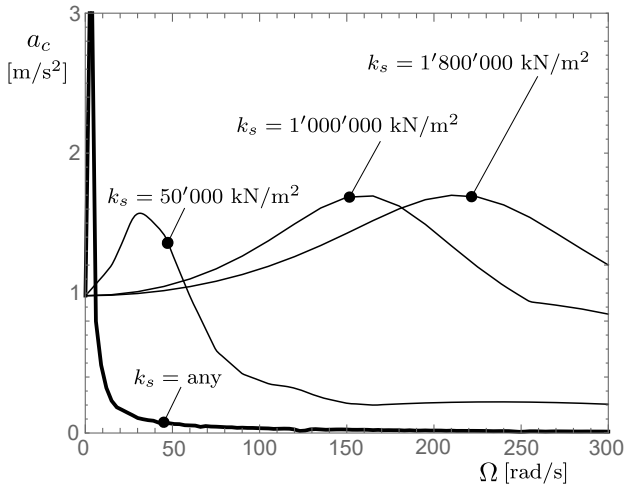

Fig. 7 Frequency-response curves of the acceleration a_c: Comparisons between isolated system without HMDI (thick lines) and non-isolated system (thin lines), under different soil conditions. Parameters: $m_{c1} = 1'407.08$ kg and $C_{c1} = (0, -0.802)$ m (case (i) in Sect. 4.1), $T_{is} = 2.0$ s.

Figure 7 displays the three frequency-response curves of the system without internal isolation (thin lines) and those of the system with a seismically isolated internal frame (thick lines). As observed, the curves corresponding to the unprotected system are clearly distinguishable from one another, indicating a strong dependence of the response on soil properties. In contrast, the three frequency-response curves of the internally isolated system are almost perfectly superimposed, revealing a very limited sensitivity of the response to soil characteristics. It is worth noting that such substantial independence from soil properties is also observed in base-isolated frame structures, where the underlying soil is often idealized as infinitely rigid.

Finally, it is useful to clarify that a parametric analysis of the soil stiffness properties is conducted exclusively in this section, with the aim of demonstrating their negligible role on the behavior of the internally isolated system. In the remainder of the paper, these properties are held constant, and in particular $k_s = 1'000'000$ kN/m^2.

5.2 Frequency-response curves to assess the role of the control parameters

To evaluate the effectiveness of different levels of content protection in utility tunnels, each of the following graphs includes three frequency-response curves. Specifically, one curve corresponds to the tunnel equipped only with seismic isolation of the internal frame (solid thin line); the second represents the internally isolated tunnel additionally equipped with a Hysteretic Mass Damper (HMD), introduced to control both the displacement and horizontal acceleration of the content (dashed thick line); the third curve refers to the internally isolated system with the HMD connected to an inerter device (HMDI), intended to further enhance the performance of the internal protection system (solid thick line).

Figure 8 presents a set of graphs, each containing the three aforementioned frequency-response curves, and accounting for a hysteretic hardening behavior of both the HMD and HMDI. Specifically, Fig. 8a corresponds to an isolation period of $T_{is} = 2.0$ s, while Fig. 8b refers to $T_{is} = 3.0$ s. In both subfigures, the graphs are arranged in rows and columns: the first row displays the frequency-response curves of the content acceleration a_c, whereas the second row shows those of the horizontal displacement u_2 of the internal frame. Each column corresponds to a different period of both the HMD and HMDI devices, denoted as T_h. Finally, in each graph, the vertical dashed reference line indicates the primary resonance peak of the internally isolated system without either HMD or HMDI, occurring at a frequency very close to the isolation frequency.

To establish a clear understanding of the key features of these graphs, a detailed description of the results in Fig. 8a is first provided. Focusing on the graphs in the middle column ($T_h = 2.0$ s), it can be observed that both the HMD and HMDI significantly reduce the acceleration a_c and the displacement u_2 at the resonance peak of the internally isolated system without additional devices (at the vertical dashed line). Specifically, the acceleration a_c is reduced by the same amount regardless of whether the HMD or HMDI is used, as the vertical dashed line intersects the frequency-response curves corresponding to the protected systems with HMD and HMDI at nearly the same point, close to the intersection of the two curves. In contrast, the reduction in displacement u_2 achieved by the HMDI is noticeably greater than that provided by the HMD.

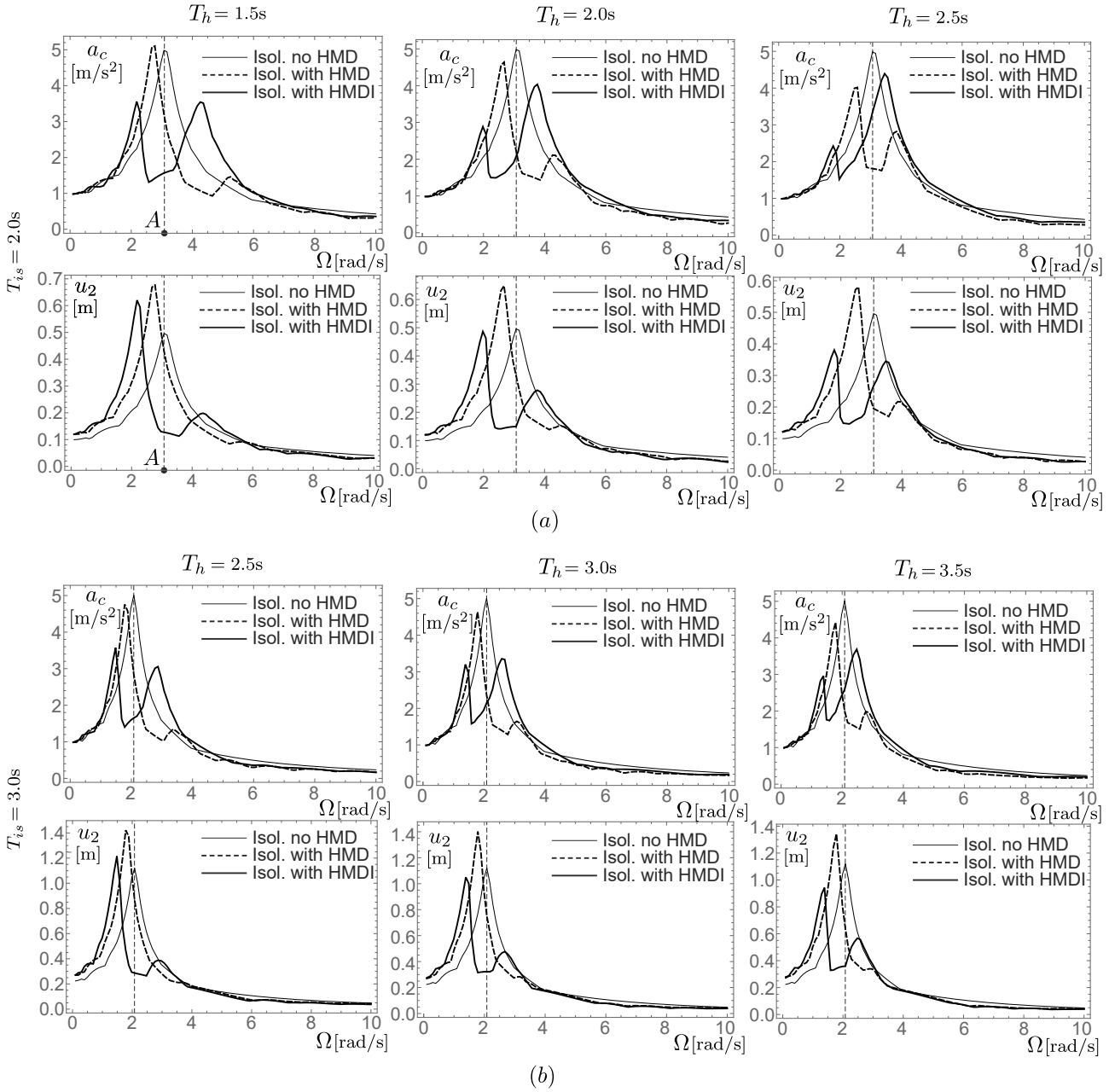

Fig. 8 Frequency-response curves of acceleration a_c and displacement u_2 for a hardening hysteretic behavior: Comparisons between isolated system without HMD (solid thin line), with HMD (dashed line) and HMDI (solid thick line), for (a) $T_{is} = 2$ s and (b) $T_{is} = 3$ s. Parameters: $m_{c1} = 1'407.08$ kg and $C_{c1} = (0, -0.802)$ m (case (i) in Sect. 4.1), $\eta_h = 0.2$, $\eta_I = 0.3$, $\beta = -0.50$, $u_y = 0.30$ m.

As general observations, the introduction of an additional device such as the HMD or HMDI enriches the dynamic behavior of the system by increasing the number of resonant peaks visible in the frequency-response curves. Acting similarly to a tuned mass damper, these devices cause the main resonant peak, originally present in the system with only internal isolation, to split into two distinct peaks, one shifted to lower frequencies and the other to higher frequencies. When properly designed, both the HMD and HMDI can significantly reduce the system's response in the vicinity of the original resonance. It is evident that the effectiveness of the protection strategy is enhanced when the HMD or HMDI not only attenuates the response compared to the system with internal isolation alone but also shifts the new resonant peaks away from the main spectral content of the excitation.

Shifting attention to the graphs in the left and right columns corresponds to considering different periods for both the HMD and HMDI devices. Specifically, in

the left column ($T_h = 1.5$ s), the best performance is achieved by the system equipped with the HMDI, as it provides the greatest reduction in both acceleration a_c and displacement u_2 at the resonance peak of the system with only internal isolation. Conversely, when the period of both the HMD and HMDI is increased to $T_h = 2.5$ s (right column), the HMDI performs worse than the system with only the HMD.

As observed, the tuning period of the HMD and HMDI devices plays a fundamental role in enhancing the system's response. The results show that the nominal tuning, in which the isolation period $T_{is} = 2.0$ s matches the period of the HMD or HMDI device ($T_h = 2.0$ s), does not lead to the best performance. In fact, the most favorable results are achieved when $T_h = 1.5$ s, a value lower than that corresponding to the nominally tuned condition.

The graphs shown in Fig. 8b refer to an internal isolation period of $T_{is} = 3.0$ s, which is greater than the one considered previously. In this case, the periods of both the HMD and HMDI are selected close to the isolation period $T_{is} = 3.0$ s in order to achieve optimal tuning conditions. The same conclusions for $T_{is} = 2.0$ s can be confirmed. In particular, the best performance of the protected system, corresponding to the maximum reduction in both acceleration a_c and displacement u_2, is achieved by the HMDI with a period of $T_h = 2.5$ s (graphs in the left column). As observed previously, the best performance is again obtained when the HMDI period is slightly shorter than the isolation period.

Figure 9 shows a set of graphs, each displaying the three frequency-response curves described earlier, considering a hysteretic softening behavior for both the HMD and HMDI. Specifically, Fig. 9a corresponds to an isolation period of $T_{is} = 2.0$ s, while Fig. 9b refers to $T_{is} = 3.0$ s. The layout of the graphs, organized in rows and columns, is the same as in Fig. 8. In each graph, a vertical dashed line marks the primary resonance peak of the internally isolated system without HMD or HMDI.

With reference to the graphs in Fig. 9a, for an isolation period of $T_{is} = 2.0$ s, it can generally be observed that both the HMD and HMDI reduce the acceleration a_c and the displacement u_2 compared to the response of the system with only internal isolation, particularly near its resonance peak. However, the effectiveness of the protection strongly depends on the tuning period of the HMD or HMDI. Specifically, for $T_h = 2.0$ s, corresponding to the nominal perfect tuning with the isolation period, the system with the HMD performs better than the one with the HMDI.

When the period of the HMD or HMDI is reduced, the HMDI achieves its best performance at $T_h = 1.0$ s, providing an almost simultaneous maximum reduction of both a_c and u_2. Similar results are observed in Fig. 9b, which refers to an isolation period of $T_{is} = 3.0$ s. Also in this case, the performance depends significantly on the tuning period of the HMD or HMDI, with the system using the HMDI and the shortest period ($T_h = 2.0$ s) again yielding the greatest simultaneous reduction in both a_c and u_2.

To summarize the results from Fig. 8 and Fig. 9, both hardening and softening hysteretic behaviors of the devices are effective and, if properly designed, can ensure optimal performance of the protected system with HMDI, outperforming both the internally isolated system alone and the system equipped with only the HMD. The main difference between hardening and softening hysteretic characteristics lies in the optimal tuning of the device period. In particular, softening hysteretic devices require shorter tuning periods for the HMDI compared to those required by hardening hysteretic devices. Finally, under nominal perfect tuning conditions, the hardening behavior ensures that the HMDI outperforms the HMD (see the middle-column graphs in Fig. 8), with the HMDI requiring only a slightly shorter period to achieve optimal performance. Conversely, under the same tuning conditions, the softening behavior leads to better performance for the system with the HMD compared to that with the HMDI (see the right-column graphs in Fig. 9). In this case, for the system with the HMDI to reach optimal performance, a more significant reduction in the device period is required.

To gain a deeper understanding of the behavior of the protected system and the improvement provided by the HMD and HMDI devices, selected time-histories are analyzed. Figure 10 presents a set of graphs illustrating these time-histories. Specifically, the first and second rows refer to systems subjected to harmonic excitations with frequency Ω, corresponding to points labeled A in Fig. 8 and B in Fig. 9, respectively. The graphs in the left and middle columns compare the acceleration a_c and the displacement u_2 obtained from the following three configurations: internally isolated system without HMD or HMDI (solid thin line); internally isolated system with HMD (dashed thick line); and internally isolated system with HMDI (solid thick line). Consistently with the frequency-response curves at points A and B, both the acceleration a_c and the displacement u_2 progressively decrease from the internally isolated system without HMD or HMDI to the system equipped with HMDI. The similarity in the maximum values of a_c for the systems with HMD and HMDI at point B (left graph in the second row of Fig. 10) is also evident from the corresponding frequency-response curves (middle graph in the first row of Fig. 9), where the vertical line passing

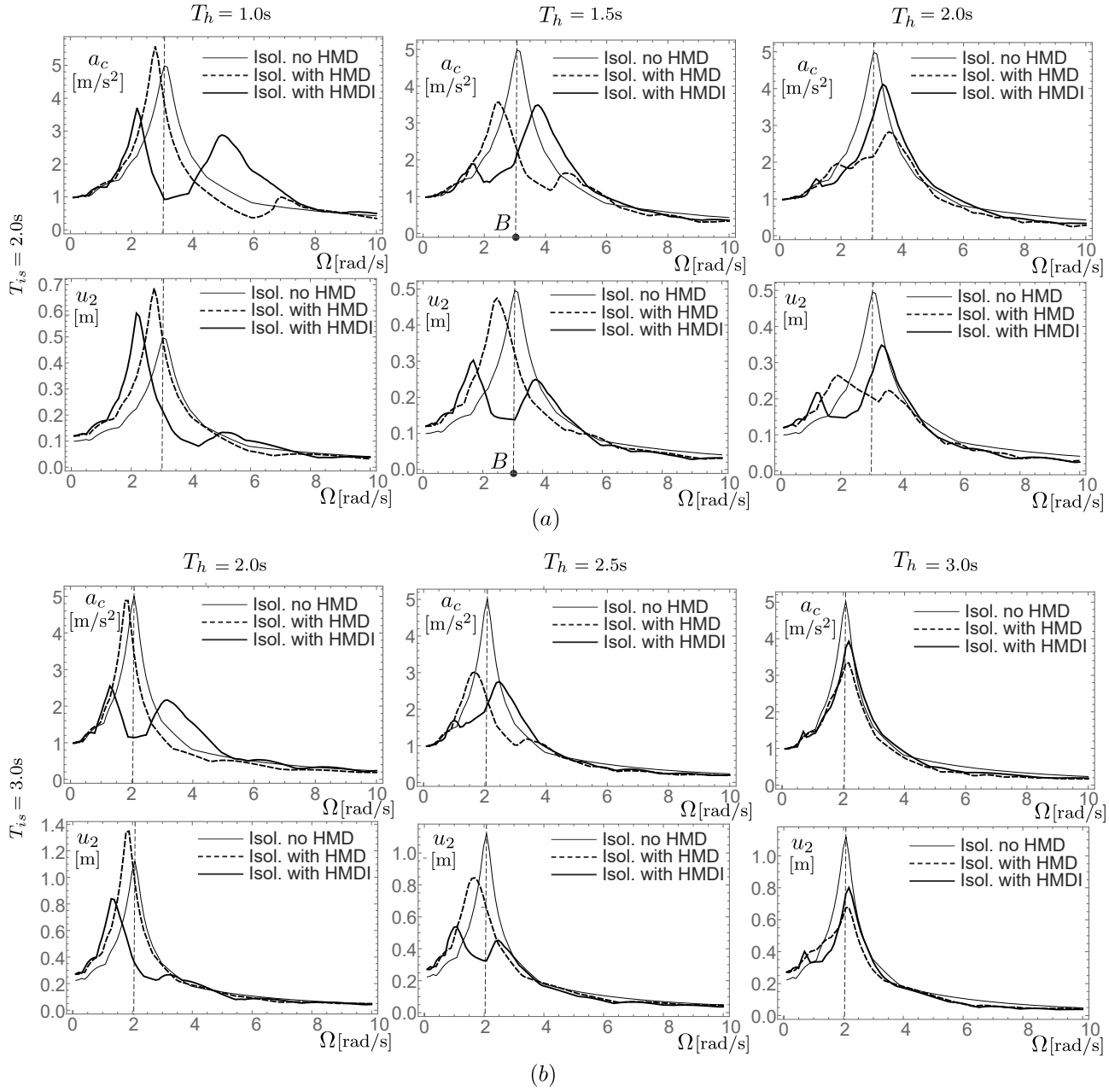

Fig. 9 Frequency-response curves of acceleration a_c and displacement u_2 for a softening hysteretic behavior: Comparisons between isolated system without HMD (solid thin line), with HMD (dashed line) and HMDI (solid thick line), for (a) $T_{is} = 2$ s and (b) $T_{is} = 3$ s. Parameters: $m_{c1} = 1'407.08$ kg and $C_{c1} = (0, -0.802)$ m (case (i) in Sect. 4.1), $\eta_h = 0.2$, $\eta_I = 0.3$, $\beta = -0.50$, $u_y = 0.30$ m.

through point B intersects the curves of the systems with HMD and HMDI at nearly the same value.

Finally, the graphs in the right column of Fig. 10 show the time-histories of the horizontal displacement u_2 of the internally isolated frame and the displacement u_h of the HMDI device. At both points A and B, the HMDI device effectively reduces accelerations and displacements by oscillating out-of-phase (at point A) or in near-perfect counter-phase (at point B) with the internal frame, thereby functioning similarly to a conventional tuned mass damper.

6 Seismic analysis

The seismic analysis is conducted by subjecting the internally isolated system, equipped with the HMDI device, to selected earthquake records while varying one or more parameters. Two performance indices are introduced: the nondimensional acceleration of the content, a_c/g,

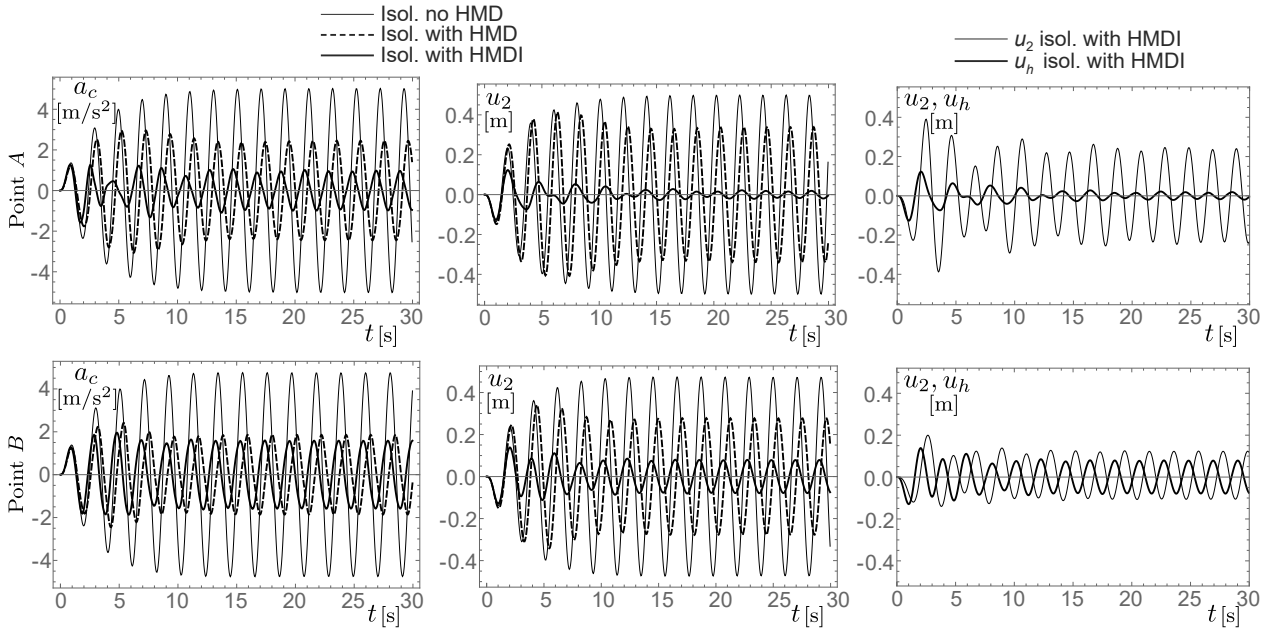

Fig. 10 Time-histories of acceleration a_c and displacement u_2 of the content and of the HMDI displacement u_h in Point A of Fig. 8 ($\Omega = 3.1$rad/s) and in Point B of Fig. 9 ($\Omega = 3.0$rad/s). Parameters: $m_{c1} = 1'407.08$ kg and $C_{c1} = (0, -0.802)$ m (case (i) in Sect. 4.1), $\eta_h = 0.2$, $\eta_I = 0.3$, $u_y = 0.30$ m.

and the nondimensional displacement of the internally isolated frame, $u_2/(2l_x)$. The results of the parametric studies are presented in two performance maps, each displaying contour plots of the respective performance indices on a specific two-parameter plane. In these maps, the earthquake record and all other parameters are held constant, except for the two parameters under investigation.

To improve readability, contour levels are represented using a grayscale scheme, where lighter shades correspond to lower values of the performance indices. Regions with lighter tones indicate better seismic performance of the protected system, reflecting reduced acceleration and displacement values.

When possible, specific reference contour levels are included within the performance maps. Two such levels are highlighted in the maps of the nondimensional acceleration a_c/g: one representing the maximum acceleration of the content in the system without internal isolation (thick dashed line), and the other corresponding to the system with only internal isolation and no HMDI device (thick dotted line). These reference contours help identify regions in the performance maps where the HMDI device outperforms both the original tunnel system and the system with only internal isolation. Additionally, a special contour level is highlighted in the maps of the nondimensional displacement $u_2/(2l_x)$, representing the maximum horizontal displacement of the internal frame in the system with only internal isolation (thick dashed line). This contour similarly aids in identifying areas where the HMDI device improves performance over the system with only internal isolation.

6.1 Earthquake records

The seismic analyses are performed using three selected earthquake records, whose time-histories and response acceleration spectra are shown in Fig. 11. The selected ground motions are listed below:

- Cristchurch, 2011, Site REHS 43.3569S, 172.6350E, REHS-01675, Christchurch Resthaven, instrument Etna-1675;
- Kobe, 1995 Japan earthquake, Takarazuka station, 0 deg, ground level, position of the station: 34.8090N, 135.3440W;
- Parkfield, 1966 California earthquake, CO2-065 recorded ground motion, station n. 013: 35.7264N, 120.2869W Cholame, Handon, array n. 2.

For clarity, each record is labeled with the underlined name in the list. The use of these three natural earthquake records is driven by the need for an initial evaluation of the protection system's performance under seismic inputs characterized by distinct spectral contents.

In this preliminary phase of the study, the earthquake records are employed without scaling to a specific design spectrum or code-based intensity level. The objective

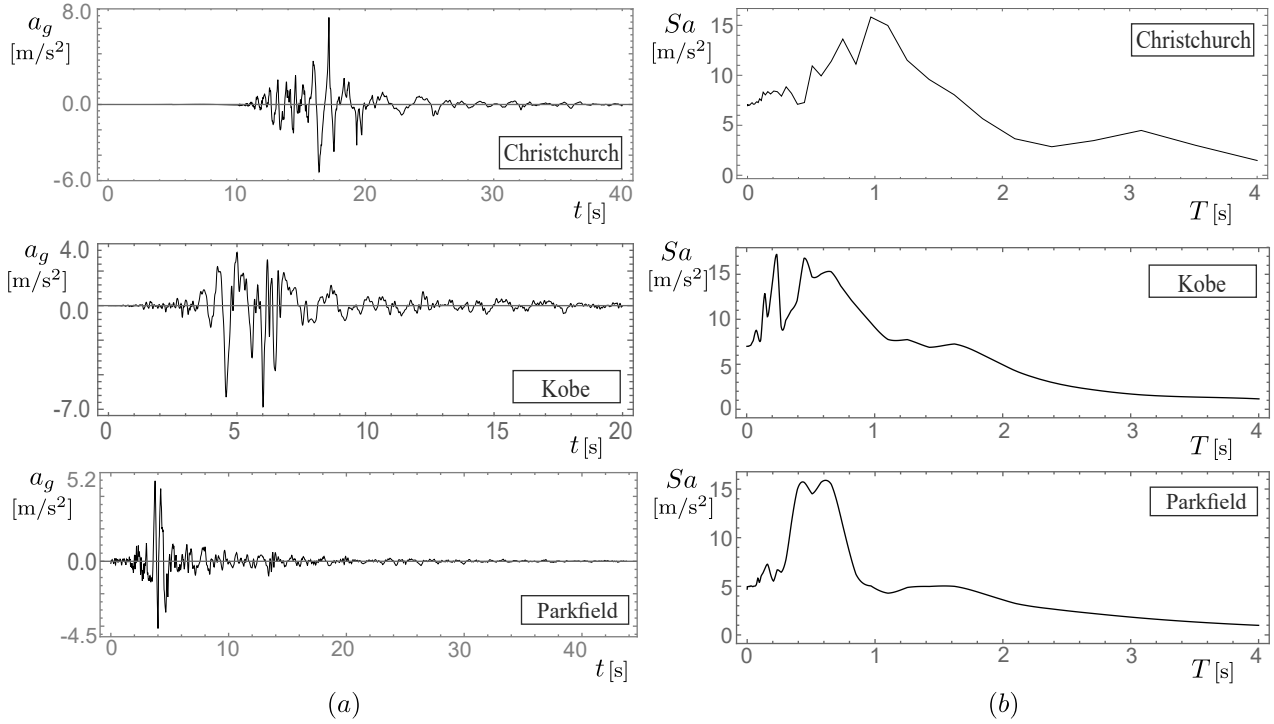

Fig. 11 Earthquake records: (a) Time-histories; (b) Response acceleration spectra.

is to qualitatively evaluate the sensitivity of the protection system to variations in seismic frequency content by using natural, unmodified ground motions, thereby preserving the inherent variability of real earthquake data. However, for a thorough assessment of practical applicability, particularly for a specific structure or site, ground motions should be selected and scaled in accordance with seismic code provisions, hazard levels, and target spectra. Future developments of this research will address these aspects, enabling a more rigorous and code-compliant evaluation of the proposed protection strategies.

6.2 The role of the parameters on the seismic response of the system

In this section, the influence of various parameters characterizing the mechanical system is investigated through the construction of performance maps. To this end, the system is always subjected to the Kobe earthquake. The system's response to the other selected ground motions will be discussed in the following section.

The first analysis aims to investigate the response of the internally isolated system equipped with the HMDI device in the parameter plane T_h and η_I, accounting for the period of the HMDI and the virtual mass of the inerter device, respectively. Figure 12 presents four performance maps referring to the isolation period $T_{is} = 2.0$s, arranged such that the two columns correspond to the acceleration and displacement maps, respectively, while the two rows refer to the hardening and softening hysteretic behaviors of the device. In the acceleration maps (left column), the thick dotted curves indicate the maximum acceleration experienced by the system with internal isolation only, as previously described. The special contour level representing the maximum acceleration of the original, unprotected system is not shown, as its value is so high that it lies outside the range displayed in both maps. Within the clearer-shaded regions bounded by the thick dotted contours, the absolute acceleration acting on the tunnel's contents is lower than that observed with internal isolation alone. Thus, within these regions, the HMDI device proves beneficial for the system's performance. Furthermore, a distinct absolute minimum of acceleration can be identified, corresponding to the configuration where the protected system achieves its best performance in terms of reduction of the acceleration a_c.

The displacement maps (right column) also reveal regions of optimal performance for the internally isolated system equipped with the HMDI device. Within the clearer-shaded areas, the system exhibits the smallest displacement of the internally isolated frame. The special contour level corresponding to the maximum displacement of the system with internal isolation alone is not shown, as the displacement values exceed the range displayed in the maps. An absolute minimum of

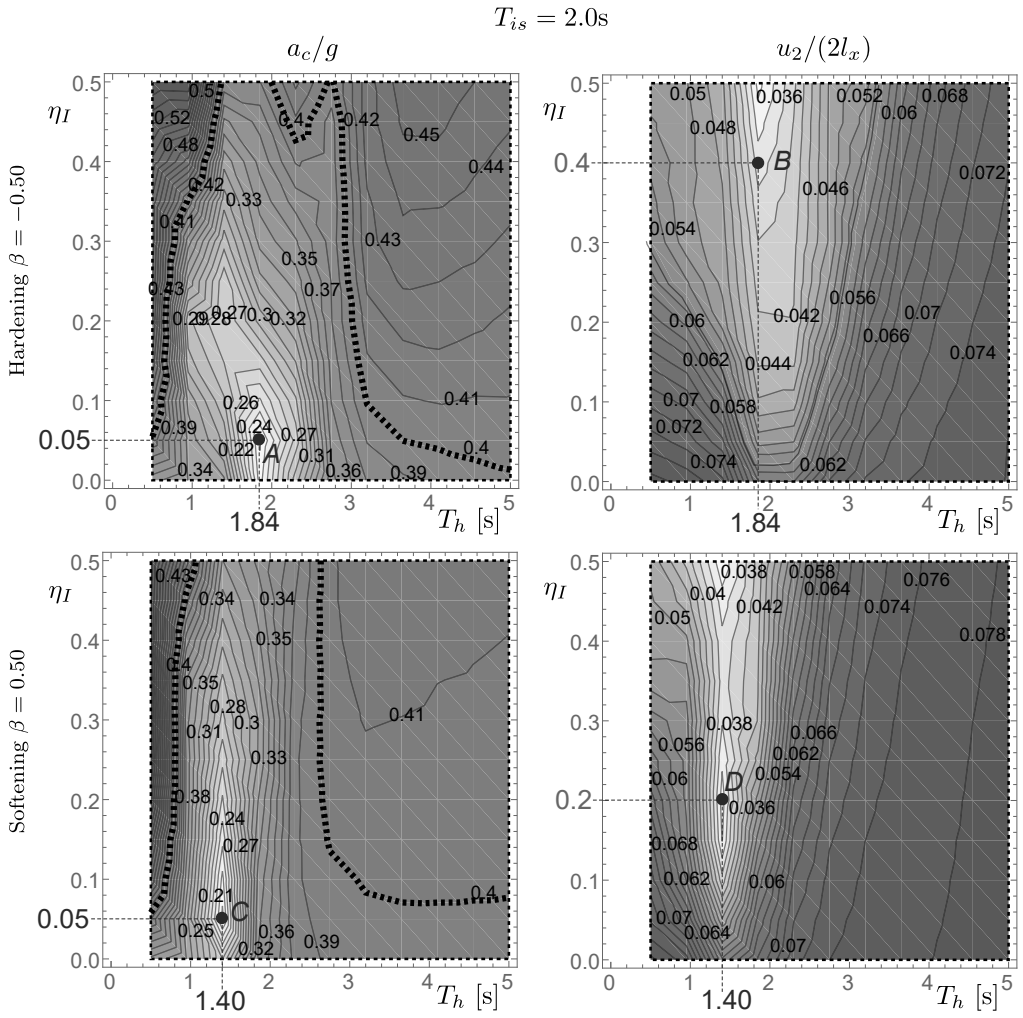

Fig. 12 Performance maps of acceleration (a_c/g) and displacement ($u_2/2l_x$) in the parameter plane (T_h-η_I), under Kobe earthquake. Parameters: $m_{c2} = 4'221.24$ kg and $C_{c2} = (1, -0.802)$ m (case (ii) in Sect. 4.1), $\eta_h = 0.1$, $u_y = 0.20$ m.

the displacement u_2 is also identifiable; however, this minimum generally does not coincide with the absolute minimum of the acceleration a_c. As a result, it is not possible to identify a single combination of the parameters T_h and η_I that simultaneously minimizes both response quantities. Therefore, when selecting these parameters during the design process, it is crucial to determine which response, acceleration or displacement, requires greater reduction.

Finally, the comparison between the maps in the first and second rows highlights the influence of the hysteretic device's behavior, either hardening or softening, on the response of the protected system. In general, the hardening behavior enlarges the region where the acceleration is reduced compared to the system with only internal isolation. Furthermore, the hardening behavior is more effective in reducing displacements than the softening one. On the other hand, the softening behavior performs better in reducing acceleration. Consistently with the previously discussed frequency-response curves, the best performance of the hardening hysteretic devices is achieved for longer HMDI periods than those required in the softening case.

Similar performance maps are presented in Fig. 13, with the only difference that they refer to a larger isolation period, $T_{is} = 3.0$ s. In this figure as well, the layout of the performance maps places the acceleration and displacement results in the left and right columns, respectively, while the first and second rows correspond to the hardening and softening hysteretic characteristics of the device. In the acceleration maps (left column), the thick dotted lines represent the peak acceleration observed in the system with only internal isolation, as in the other figures. The extent of the clearer-shaded areas enclosed by these contours, indicating where the absolute acceleration on the tunnel contents is significantly reduced, is generally smaller than what is observed for $T_{is} = 2.0$ s. Nevertheless, a clear absolute minimum in

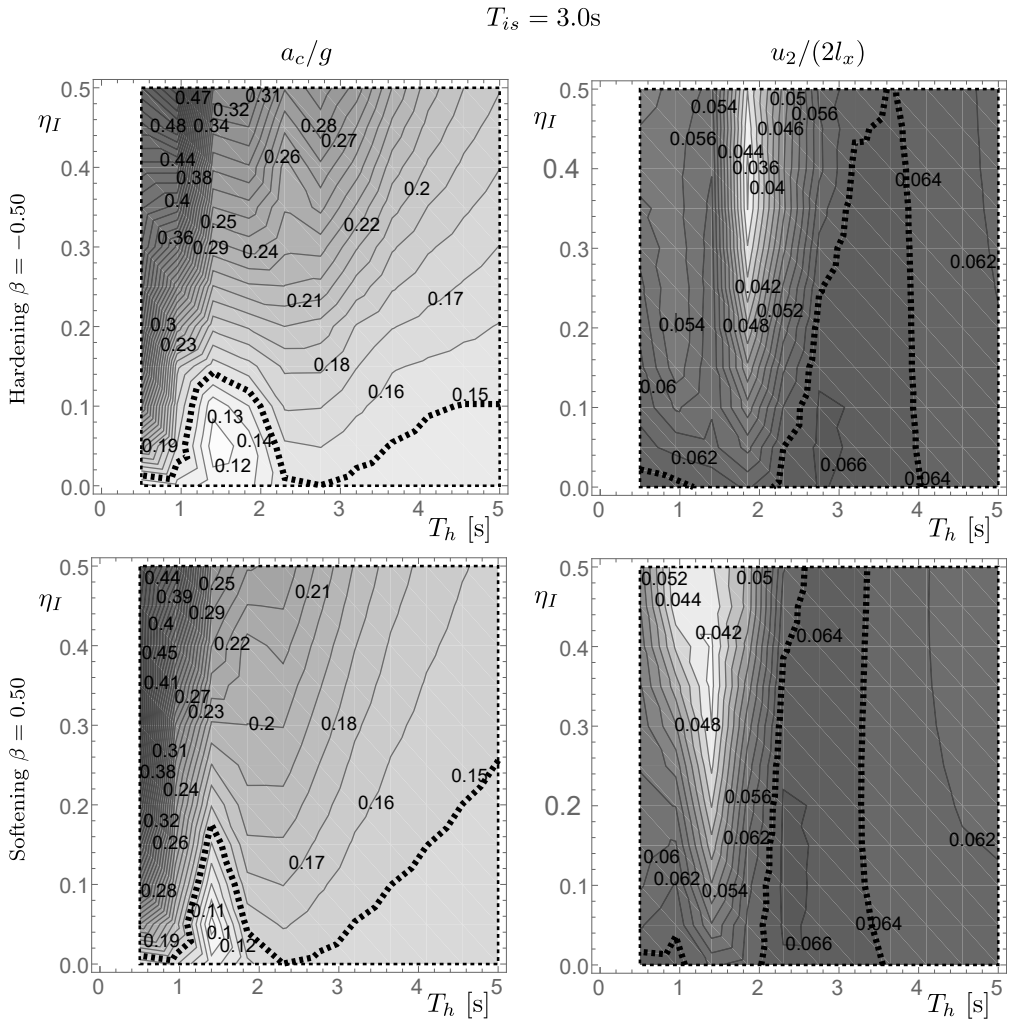

Fig. 13 Performance maps of acceleration (a_c/g) and displacement ($u_2/2l_x$) in the parameter plane (T_h-η_I), under Kobe earthquake. Parameters: $m_{c2} = 4'221.24$ kg and $C_{c2} = (1, -0.802)$ m (case (ii) in Sect. 4.1), $\eta_h = 0.1$, $u_y = 0.20$ m.

acceleration can still be identified, indicating the point of greatest reduction in a_c.

The displacement maps (right column) similarly highlight areas where the HMDI-equipped, internally isolated system performs optimally. Within the lighter regions, delimited by the thick dotted contour representing the maximum displacement of the system with internal isolation alone, the smallest values of the internal frame displacement are achieved. A clear absolute minimum of u_2 can also be observed; however, this minimum typically does not align with the absolute minimum of the acceleration a_c. Consequently, no unique pair of parameters T_h and η_I can be identified that simultaneously yields minimum values for both performance indices.

A comparison between the first and second row maps underscores the influence of the hysteretic behavior of the device. It is evident that a hardening hysteresis expands the region in which the acceleration is lower than that observed in the system with internal isolation alone. Additionally, hardening devices are generally more effective in mitigating displacement responses. In contrast, devices with softening hysteresis demonstrate greater efficiency in reducing acceleration. Finally, consistent with the frequency-response analysis, the optimal performance of hardening-type HMDI devices is typically achieved at longer periods compared to the softening case.

As a final remark, it is worth noting that, for longer isolation periods, a design strategy aimed at minimizing the displacement u_2, by selecting the parameters corresponding to the absolute minimum in the $u_2/(2l_x)$ performance map, may result in acceleration values a_c that lie outside the clearer-shaded region, where the HMDI provides better performance than the system with internal isolation alone. Nevertheless, even in such cases, the resulting acceleration remains lower than that observed for the isolation period $T_{is} = 2.0$ s discussed earlier.

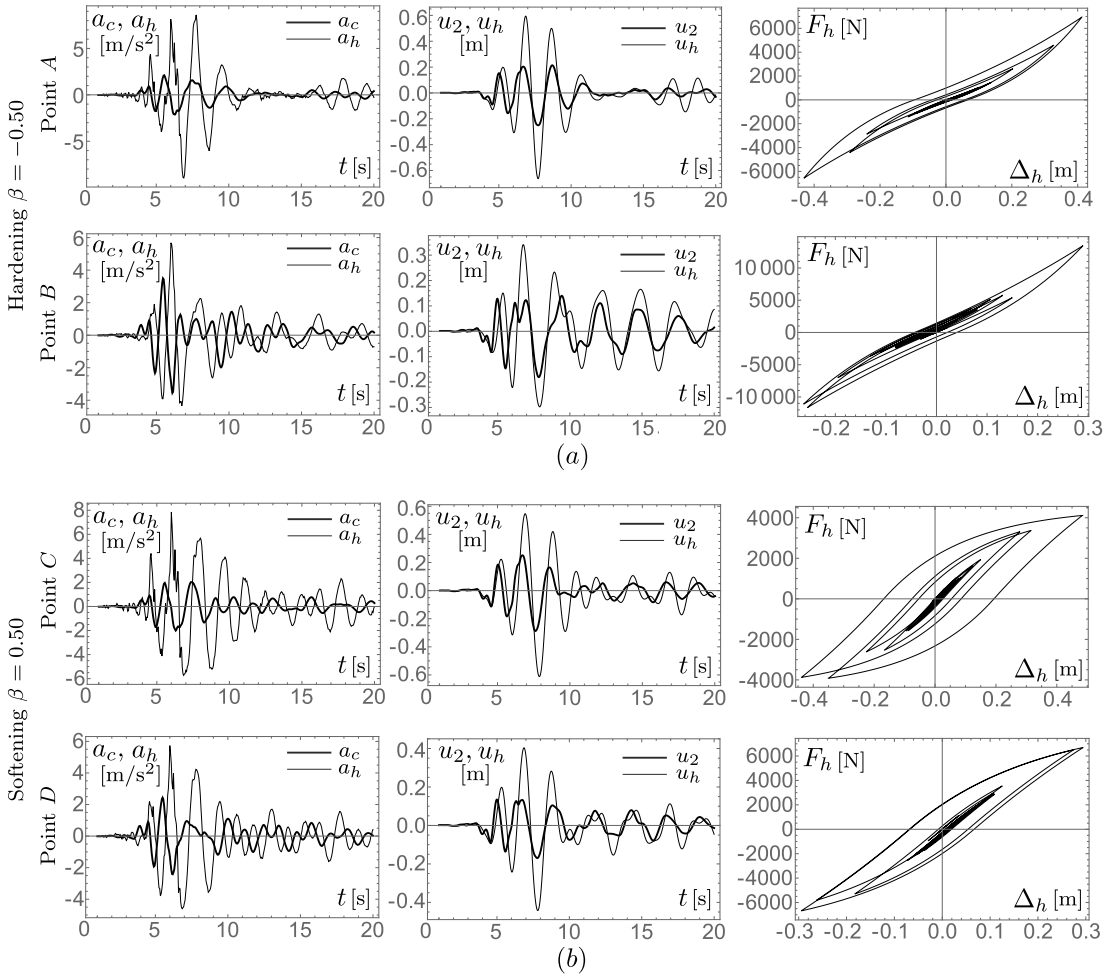

Fig. 14 Time-histories of the accelerations a_c, a_h and the displacements u_2, u_h in point A, B, C, D of Fig. 12.

To gain a deeper understanding of the behavior of the protected system and the enhancements provided by the HMDI devices, selected time-histories are examined. Figure 14 presents a series of graphs depicting these time-histories, corresponding to four representative systems identified as points A, B, C, and D in Fig. 12. Specifically, points A and B, whose time-histories are shown in the first and second rows of Fig. 12a, respectively, pertain to the hardening behavior of the hysteretic device. In contrast, points C and D, illustrated in the first and second rows of Fig. 12b, correspond to the softening hysteretic behavior. The left and middle columns of Fig. 12 display graphs, each containing two distinct time-histories. Specifically, the plots in the first column show the acceleration time-histories of the content, a_c (thick line), and of the HMDI device, a_h (thin line). The graphs in the second column illustrate the displacement time-histories of the internally isolated frame, u_2 (thick line), and of the HMDI device, u_h (thin line). Finally, the third column presents the hysteretic cycles of the HMDI device.

Points A and B correspond to the absolute minimum of the acceleration a_c and the absolute minimum of the displacement u_2, respectively. The same criterion is adopted for the selection of points C and D. In all these cases, both the acceleration a_h and the displacement u_h of the HMDI device exhibit a noticeable out-of-phase motion with respect to a_c and u_2, particularly during the initial oscillations. As a result, the HMDI behaves similarly to a tuned mass damper, effectively contributing to the reduction of both accelerations and displacements. Finally, as expected, the analysis of the hysteretic cycles (third column) confirms the hardening and softening behavior of the hysteretic device.

To further investigate the influence of the hysteretic behavior of the HMDI device, the performance indices a_c/g and $u_2/(2l_x)$ are mapped in a different parameter plane. In this case, the two varying parameters are the HMDI period T_h and the hysteresis parameter β, while all other parameters are held constant. As explained in Sect. 2.3, the parameter β governs the hysteretic characteristics of the device. By varying β from nega-

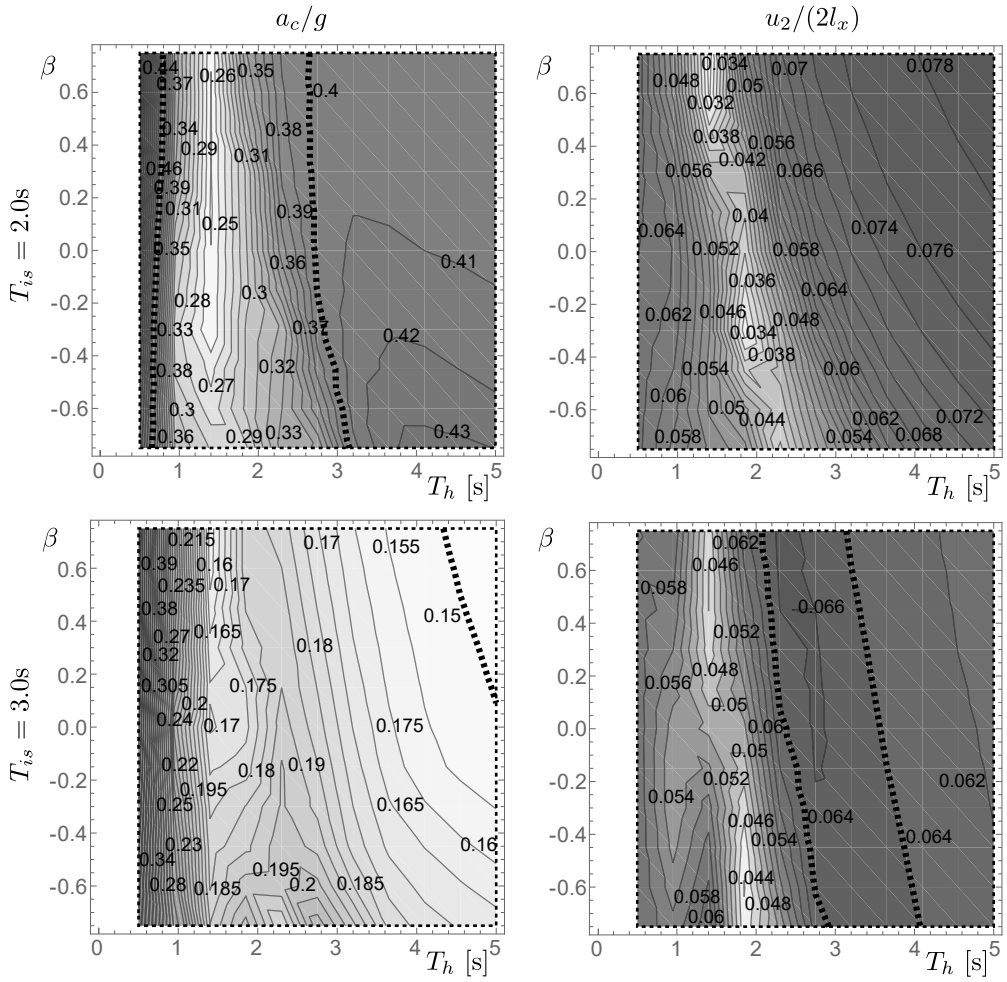

Fig. 15 Performance maps of acceleration (a_c/g) and displacement ($u_2/2l_x$) in the parameter plane (T_h-β), under Kobe earthquake. Parameters: $m_{c2} = 4'221.24$ kg and $C_{c2} = (1, -0.802)$ m (case (ii) in Sect. 4.1), $\eta_h = 0.1$, $\eta_I = 0.2$, $u_y = 0.20$ m.

tive (corresponding to hardening behavior) to positive values (representing softening behavior), the effect of the hysteresis type on the system performance can be systematically evaluated. Figure 15 presents the performance maps of the indices a_c/g and $u_2/(2l_x)$, shown in the two columns. The maps refer to two different isolation periods, $T_{is} = 2.0$s and $T_{is} = 3.0$s, which are arranged in the first and second row, respectively.

In the case of $T_{is} = 2.0$ s (maps in the first row), clearly distinguishable clearer-shaded regions appear in both performance maps, indicating where the system exhibits optimal behavior. In particular, in the acceleration map, the clearer-shaded region is bounded by the well-known thick dotted curve, thereby ensuring performance superior to that of the system with internal isolation alone. Furthermore, predominantly visible in the displacement map, the clearer-shaded region is inclined such that softening hysteretic behaviors (positive β) correspond to shorter periods T_h, whereas hardening hysteretic behaviors correspond to longer periods T_h, as previously discussed. Finally, even in the displacement map, two absolute minima of the displacement u_2 can be clearly identified, highlighting the significant influence of the HMDI device's hysteretic behavior on the protected system.

In the case of $T_{is} = 3.0$s (maps in the second row), the acceleration performance map (left map) shows that the optimal, clearer-shaded region lies to the right of the thick dotted curve. This indicates that, across most of the parameter plane, the acceleration a_c is higher than in the system with internal isolation alone. The behavior of the displacement u_2 is different. In the corresponding performance map (right map), a clearer-shaded region bounded by the thick dotted curve indicates where displacements are smaller than those in the system with only internal isolation. However, if the design goal is to minimize u_2 by selecting parameters corresponding to an absolute minimum in the displacement map, the resulting acceleration a_c is however lower than that achieved with an isolation period of $T_{is} = 2.0$s. In summary, a

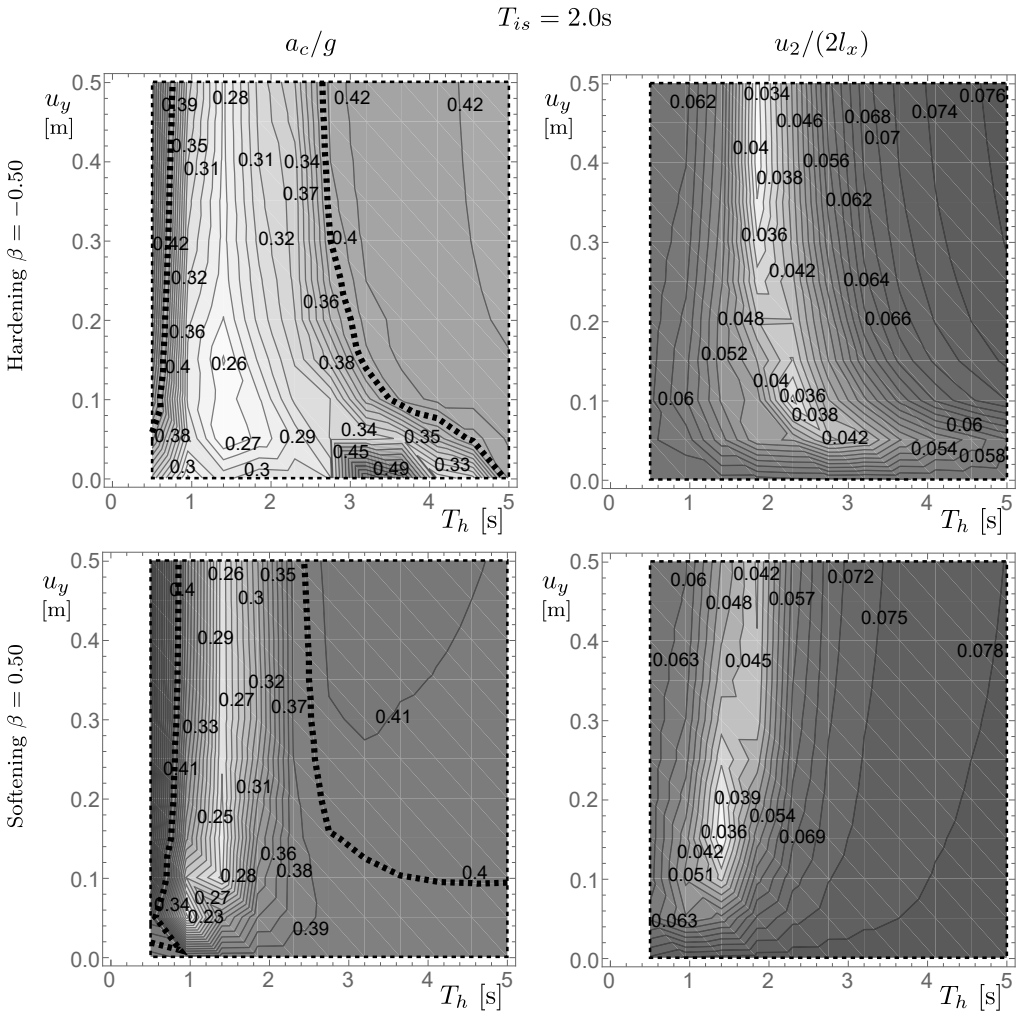

Fig. 16 Performance maps of acceleration (a_c/g) and displacement ($u_2/2l_x$) in the parameter plane (T_h-u_y), under Kobe earthquake. Parameters: $m_{c2} = 4'221.24$ kg and $C_{c2} = (1, -0.802)$ m (case (ii) in Sect. 4.1), $\eta_h = 0.1$, $\eta_I = 0.2$.

longer isolation period proves more effective primarily in reducing the displacement u_2. Although the system with only internal isolation may perform better, the acceleration a_c generally remains lower than that obtained with a shorter isolation period.

Finally, to better understand the role of the yielding displacement u_y of the hysteretic device, the performance indices a_c/g and $u_2/(2l_x)$ are mapped over the parameter plane $T_h - u_y$, while keeping all other parameters fixed. The acceleration and displacement performance maps are shown in the first and second columns of Fig. 16, respectively. Conversely, the maps in the first and second rows correspond to the hardening and softening hysteretic behaviors, respectively. Similarly to the previously discussed maps, clearer-shaded regions bounded by thick dotted curves appear only in the displacement maps. The clearness of these regions, which indicates the best performance of the protected system, depends significantly on the yielding displacement u_y. Therefore, to achieve optimal system performance, a careful selection of u_y is also recommended.

6.3 Seismic performance of the protected system under additional ground motions

To evaluate the effectiveness of the proposed protection method against transverse seismic effects acting on a utility tunnel, performance maps are generated for the two additional, selected ground motions: Christchurch and Parkfield.

Figure 17 presents four performance maps for an isolation period of $T_{is} = 2.0$ s, obtained by exciting the system with the Christchurch earthquake. The left and right columnss display acceleration and displacement maps, respectively, while the first and second rows correspond to hardening and softening hysteretic behaviors. In the upper acceleration maps (left column), the thick dotted curves indicate the maximum acceleration ex-

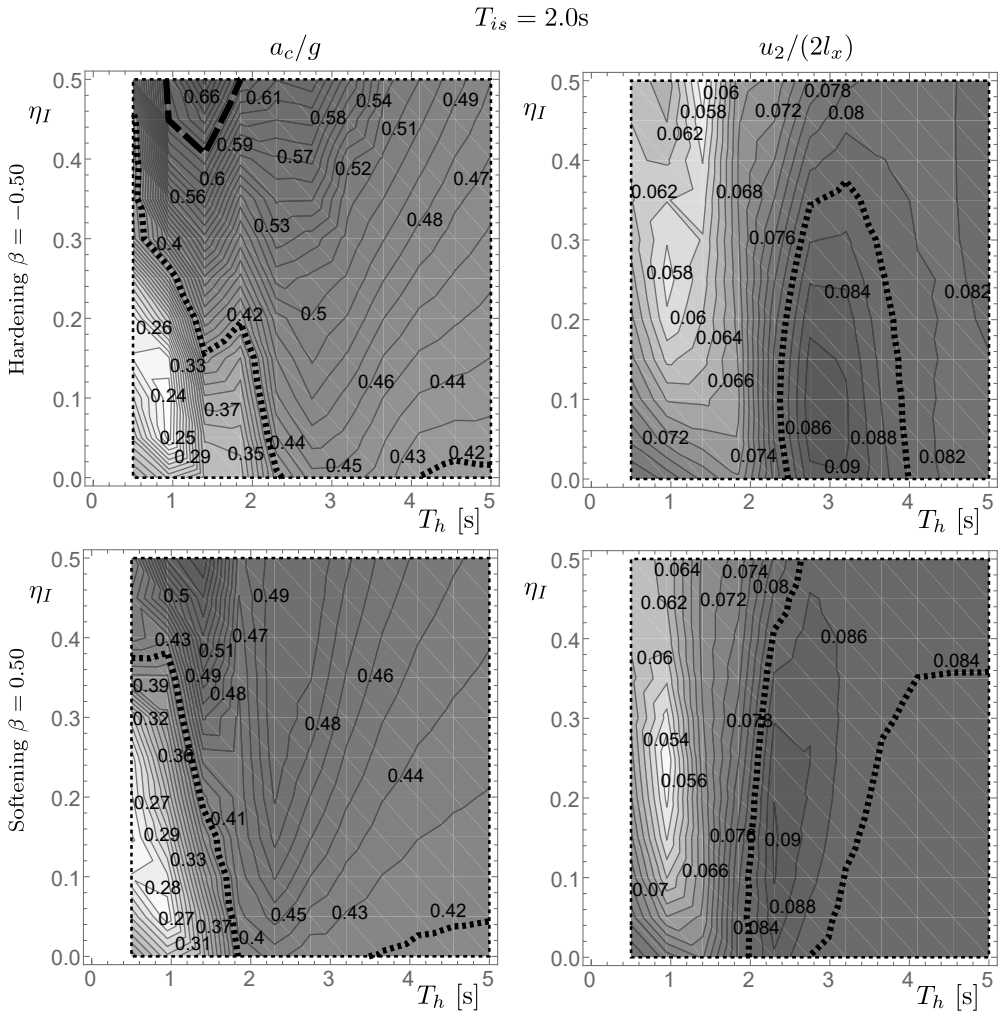

Fig. 17 Performance maps of acceleration (a_c/g) and displacement ($u_2/2l_x$) in the parameter plane (T_h-η_I), under Cristchurch earthquake. Parameters: $m_{c2} = 4'221.24$ kg and $C_{c2} = (1, -0.802)$ m (case (ii) in Sect. 4.1), $\eta_h = 0.1$, $u_y = 0.20$ m.

perienced by the system with internal isolation only, as previously described. Additionally, the thick dashed curve represents the maximum acceleration affecting the contents in the fully unprotected system. The presence of the dashed curve requires greater attention in selecting the design parameters, as it indicates that, in some cases, the acceleration a_c of the protected system could be higher than that of the unprotected one. For the Christchurch seismic event, the size of the clearer-shaded region in the acceleration map is noticeably smaller than that observed for the Kobe earthquake (see Fig. 12). In contrast, the displacement maps do not show any significant differences compared to those for the Kobe event. However, within the clearer-shaded region of the acceleration map, despite its limited extent, the displacement performance remains satisfactory. In fact, the clearer-shaded regions in both maps are sufficiently overlapped to each other, suggesting that it is possible to select design parameters that effectively reduce both a_c and u_2.

Finally, Figure 18 displays four performance maps for a system with an isolation period of $T_{is} = 2.0$ s, subjected to the Parkfield earthquake. The performance maps are arranged as in the previous figure, so that the left and right columns show the acceleration and displacement maps, respectively, while the two rows distinguish between hysteretic hardening behavior on the top and hysteretic softening behavior on the bottom. In this case, both acceleration maps (left column) not only display the thick dotted curves, which indicate the maximum acceleration experienced by the system with internal isolation only, but also include the thick dashed curves representing the peak acceleration affecting the contents in the fully unprotected system. Therefore, greater care in selecting the design parameters is required compared to the Christchurch earthquake. The clearer-shaded regions in both performance maps, for

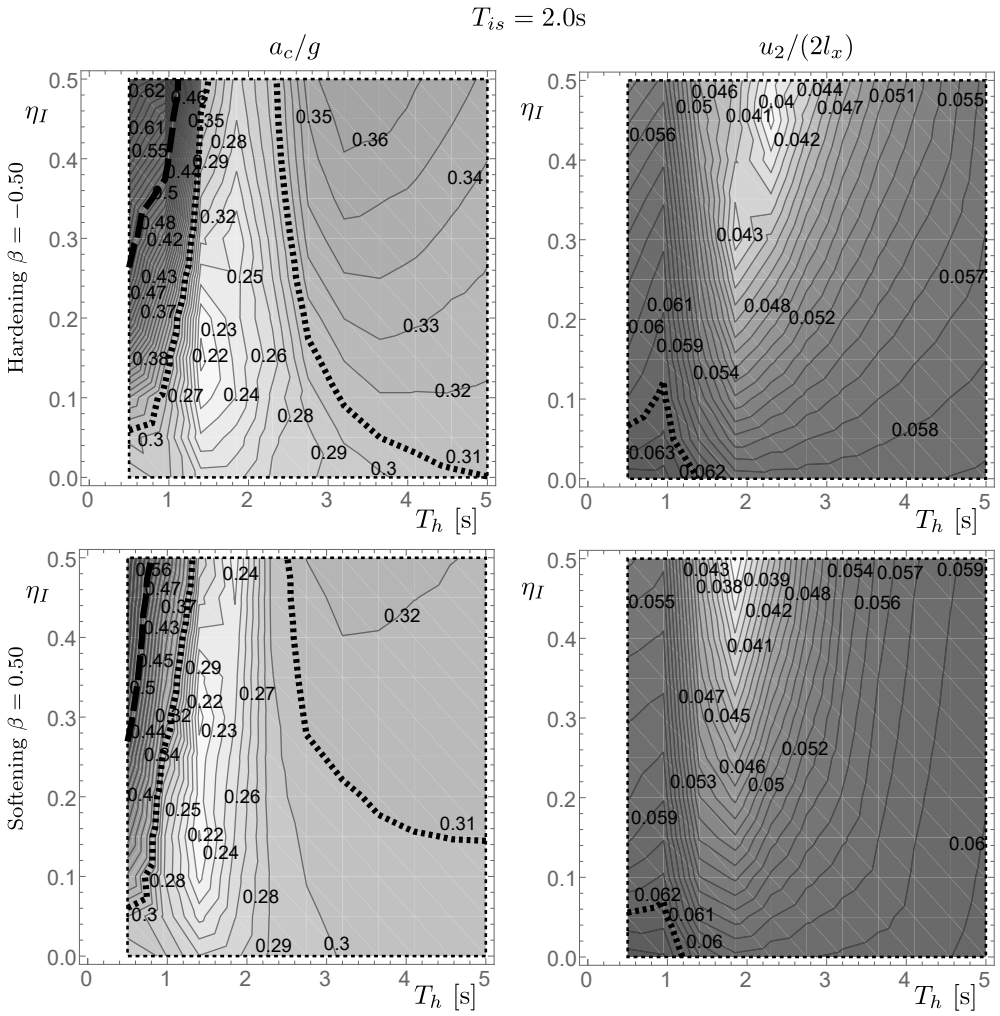

Fig. 18 Performance maps of acceleration (a_c/g) and displacement ($u_2/2l_x$) in the parameter plane (T_h-η_I), under Parkfield earthquake. Parameters: $m_{c2} = 4'221.24$ kg and $C_{c2} = (1, -0.802)$ m (case (ii) in Sect. 4.1), $\eta_h = 0.1$, $u_y = 0.20$ m.

both hardening and softening hysteretic behaviors, overlap across a common area of the parameter plane. This overlap facilitates the selection of design parameters that effectively reduce both a_c and u_2.

7 Conclusions

This study has developed and assessed protection strategies to reduce the impact of transverse seismic excitation on the internal components of utility tunnels. The proposed solution incorporates internal support frames designed to host the pipelines, which are mechanically decoupled from the tunnel structure through visco-elastic isolators. These frames have been enhanced with advanced vibration control devices, namely Hysteretic Mass Damper Inerters.

A simplified analytical model with a reduced number of degrees of freedom has been formulated. In this model, the tunnel is represented as a rigid body within its cross-sectional plane, interacting with the surrounding ground, idealized as a compression-only elastic medium. The internal equipment is mounted on a rigid frame, which is allowed to move only horizontally relative to the tunnel and is connected to it by four linear visco-elastic elements. An HMDI has been attached to one corner of the frame to augment energy dissipation and improve dynamic and sesimic response control.

The analytical model was validated against a finite element benchmark, demonstrating strong agreement and confirming its reliability for preliminary design and rapid parametric studies. To assess the proposed mitigation strategy, frequency-domain analyses under harmonic loading were conducted, highlighting the influence of isolation and control systems on the system's dynamic behavior. Finally, extensive time-history simulations were carried out using a suite of representative seismic records; the results were synthesized into performance response maps, indicating that the proposed configuration

can effectively enhance the seismic performance of utility tunnel contents under realistic earthquake scenarios.

The main novelties, key findings, and conclusions of this study are summarized as follows:

- A protection strategy combining an internally base-isolated frame supporting the pipelines and an additional control through an HMDI device has been proposed for the first time.
- It has been found that the proposed method significantly reduces the absolute acceleration acting on the pipelines, even with short periods of internal base isolation.
- Increasing the isolation period further improves the performance of the controlled system; however, the additional reduction in absolute acceleration on the pipelines comes at the cost of a significant increase in the displacement of the internally isolated frame.
- The use of the HMDI effectively reduces the displacement of the internally isolated frame and further decreases the absolute acceleration on the pipelines across a wide range of parameter values.
- The parameters characterizing the hysteretic behavior of the HMDI, such as the softening/hardening response and the yielding displacement, play an important role in the response of the controlled system and have been thoroughly investigated.
- The responses of the controlled systems with softening or hardening behavior are relatively similar; in general, the softening behavior is more effective in reducing the acceleration on the pipelines, whereas the hardening behavior provides better control of the displacements of the internally isolated frame.

Funding This work is funded by the European Union - Next Generation EU, Mission 4, Component 2, Investment 1.1, in the framework of the project PRIN 2022 PNRR, "P2022ZT5X5 - Smart Under-Ground Infra-Structures for Secure Communities and Post-Disaster Emergency Response: Eco-Friendly Seismic Protection Solutions" (CUP: E53D2301762 0001, University of L'Aquila).

Data availability Data will be made available on request.

Conflict of interest The authors have no relevant financial or non-financial interests to disclose.

Author Contributions Simona Di Nino: Writing - original draft, Writing - review & editing, Visualization, Software, Methodology, Investigation, Validation, Supervision, Conceptualization. Lorenzo Mancini: Writing - original draft, Writing - review & editing, Visualization, Software, Methodology, Investigation, Validation. Manuel Ferretti: Writing - original draft, Writing - review & editing, Visualization, Software, Methodology, Investigation, Validation, Supervision, Conceptualization. Angelo Di Egidio: Writing - original draft, Writing - review & editing, Visualization, Software, Methodology, Investigation, Validation, Supervision, Conceptualization.

References

1. Y. Luo, A. Alaghbandrad, T.K. Genger, and A. Hammad. History and recent development of multi-purpose utility tunnels. *Tunnelling and Underground Space Technology*, 103:103511, 2020.
2. T.T. Wang, O.L. A. Kwok, and F.S. Jeng. Seismic response of tunnels revealed in two decades following the 1999 chi-chi earthquake (mw 7.6) in taiwan: A review. *Engineering Geology*, 287:106090, 2021.
3. Y.M. Hashash, J.J. Hook, B. Schmidt, and J. I.C. Yao. Seismic design and analysis of underground structures. *Tunnelling and underground space technology*, 16(4):247–293, 2001.
4. J.N. Wang and G. Munfakh. Seismic design of tunnels. *WIT Transactions on the Built Environment*, 57, 2001.
5. J. Lu, J. Luo, X. Huang, J. Hong, Y. Lu, and F. Zhou. Study on deformation patterns of tunnel isolation layers and seismic response of a shield tunnel. *Soil Dynamics and Earthquake Engineering*, 187:108998, 2024.
6. J. Chen, X. Shi, and J. Li. Shaking table test of utility tunnel under non-uniform earthquake wave excitation. *Soil Dynamics and Earthquake Engineering*, 30(11):1400–1416, 2010.
7. G. Tang, Y. Fang, Y. Zhong, Jie Y., B. Ruan, Y. Fang, and Q. Wu. Numerical study on the longitudinal response characteristics of utility tunnel under strong earthquake: a case study. *Advances in Civil Engineering*, 2020(1):8813303, 2020. Article ID 8813303.
8. J. Liang, J. Zhang, B. Dong, A. Xu, and Z. Ba. Shaking table tests on the seismic performance of prefabricated t-shaped cross utility tunnel. In *Structures*, volume 58, page 105516. Elsevier, 2023.
9. H. Chen, J. Liang, D. Li, and Z. Ba. Transverse seismic analysis method of underground interchange prefabricated utility tunnel. In *Structures*, volume 68, page 107112. Elsevier, 2024.
10. Z. Wang, L. Chang, H. Ma, L. Zhu, G. Cui, H. Shan, and Z. He. Seismic isolation technology of shallow buried large section utility tunnel with soft soils in seismically vulnerable area. *Frontiers in Earth Science*, 12:1351978, 2024.
11. Q. Sun, Y. Xue, and M. Hou. Geotechnical seismic isolation system to protect cut-and-cover utility tunnels using tire-derived aggregates. *Soil Dynamics and Earthquake Engineering*, 176:108354, 2024.
12. W. Liu and Q. Wu. Comparison between the seismic performance of buried pipes and pipes in a utility tunnel. *Computer Modeling in Engineering & Sciences*, 123(2):661–690, 2020.
13. J. Li, Z. Zhong, K. Bi, and H. Hao. Seismic fragility assessment of utility tunnel and internal pipeline system. *Tunnelling and Underground Space Technology*, 158:106441, 2025.
14. A. Tang, Z. Gai, A. Wen, and H. You. Seismic isolation simulation of pipeline in utility tunnel. In *ICPTT 2012: Better Pipeline Infrastructure for a Better Life*, pages 1534–1544. 2012.
15. D. Huang, Z. Zong, A. Tang, Z. Huang, and Q. Liu. Dynamic response and vibration isolation of pipes inside a utility tunnel passing through nonhomogeneous soil under seismic action. *Soil Dynamics and Earthquake Engineering*, 163:107522, 2022.
16. A. Contento and A. Di Egidio. Investigations into the benefits of base isolation for non-symmetric rigid blocks. *Earthquake engineering & structural dynamics*, 38(7):849–866, 2009.
17. A. Contento and A. Di Egidio. On the use of base isolation for the protection of rigid bodies placed on a multi-storey frame under seismic excitation. *Engineering Structures*, 62:1–10, 2014.

18. C. Fabrizio, A. M. de Leo, and A. Di Egidio. Tuned mass damper and base isolation: A unitary approach for the seismic protection of conventional frame structures. *Journal of Engineering Mechanics*, 145(4):04019011, 2019.
19. S. Di Nino and A. Luongo. Nonlinear aeroelastic behavior of a base-isolated beam under steady wind flow. *International Journal of Non-Linear Mechanics*, 119:103340, 2020.
20. S. Di Nino, D. Zulli, and A. Luongo. Nonlinear dynamics of an internally resonant base-isolated beam under turbulent wind flow. *Applied Sciences*, 11(7):3213, 2021.
21. S. Di Nino and A. Luongo. Nonlinear dynamics of a base-isolated beam under turbulent wind flow. *Nonlinear Dynamics*, 107(2):1529–1544, 2022.
22. A. Di Egidio and A. Contento. Improvement of the dynamic and seismic behaviour of rigid block-like structures by a hysteretic mass damper coupled with an inerter. *Applied Sciences*, 12(22):11527, 2022.
23. A. Di Egidio and A. Contento. Seismic benefits from coupling frame structures with a hysteretic mass damper inerter. *Applied Sciences*, 13(8):5017, 2023.
24. L. Marian and A. Giaralis. Optimal design of a novel tuned mass-damper–inerter (tmdi) passive vibration control configuration for stochastically support-excited structural systems. *Probabilistic Engineering Mechanics*, 38:156–164, 2014.
25. A. Giaralis and F. Petrini. Wind-induced vibration mitigation in tall buildings using the tuned mass-damper-inerter. *Journal of Structural Engineering*, 143(9):04017127, 2017.
26. D. Patsialis, A.A. Taflanidis, and A. Giaralis. Tuned-mass-damper-inerter optimal design and performance assessment for multi-storey hysteretic buildings under seismic excitation. *Bulletin of Earthquake Engineering*, 21(3):1541–1576, 2023.
27. T. Konar and A. D. Ghosh. Tuned mass damper inerter for seismic control of multi-story buildings: Ten years since inception. In *Structures*, volume 63, page 106459. Elsevier, 2024.
28. N. Carpineto, W. Lacarbonara, and F. Vestroni. Hysteretic tuned mass dampers for structural vibration mitigation. *Journal of Sound and Vibration*, 333(5):1302–1318, 2014.
29. A. Boccamazzo, B. Carboni, G. Quaranta, and W. Lacarbonara. Seismic effectiveness of hysteretic tuned mass dampers for inelastic structures. *Engineering Structures*, 216:110591, 2020.
30. Y. Hui, Z.Q. Yang, Q. Ruan, K. Li, and L. Bao. Nonlinear dynamic characteristics of a hysteretic tmd and its application on a tall building. *Journal of Building Engineering*, 65:105671, 2023.
31. R. Ma, K. Bi, and H. Hao. Inerter-based structural vibration control: A state-of-the-art review. *Engineering Structures*, 243:112655, 2021.
32. R. Bouc. Forced vibrations of mechanical systems with hysteresis. In *Proc. of the Fourth Conference on Nonlinear Oscillations, Prague, 1967*, 1967.
33. R. Bouc. Modele mathematique d'hysteresis. *Acustica*, 21:16–25, 1971.
34. Y.K. Wen. Method for random vibration of hysteretic systems. *Journal of the engineering mechanics division*, 102(2):249–263, 1976.
35. F. Ma, H. Zhang, A. Bockstedte, G. C. Foliente, and P. Paevere. Parameter analysis of the differential model of hysteresis. *Journal of Applied Mechanics*, 71(3):342–349, 2004.
36. M. C. Constantinou and M. A. Adnane. *Dynamics of soil-base-isolated-structure systems: evaluation of two models for yielding systems. Report to NSAF*. Department of Civil Engineering, Drexel University, Philadelphia, 1987.
37. M. C. Smith. The inerter: a retrospective. *Annual Review of Control, Robotics, and Autonomous Systems*, 3(1):361–391, 2020.
38. D. Younesian, A. Hosseinkhani, H. Askari, and E. Esmailzadeh. Elastic and viscoelastic foundations: a review on linear and nonlinear vibration modeling and applications. *Nonlinear Dynamics*, 97(1):853–895, 2019.
39. MOHURD-China and AQSIQ-China. *GB 50010-2010 (Modified in 2015) Code for Design of Concrete Structures*. Ministry of Housing and Urban-Rural Development of the People's Republic of China, 2015. National Standard of the People's Republic of China.
40. Oppo Srl. HEB Beams with Parallel Wide Flanges - Dimensional Tables (in Italian), 2025. Available at: `https://www.oppo.it/tabelle/profilati_heb.htm`.
41. B. M. Das and N. Sivakugan. *Principles of foundation engineering*. Cengage learning, 2018.
42. GeoStru. Soil Reaction Coefficient or Winkler Coefficient (in Italian), 2023. Available at: `https://www.geostru.eu/blog/2023/02/25/coefficiente-di-reazione-del-terreno-o-coefficiente-di-winkler/?lang=ro`.

A Details on the Derivation of the Equations of Motion

This section provides the detailed derivation of the equations of motion in the form of Eq. 15, with particular emphasis on the formulation of the Lagrangian and the evaluation of the virtual work associated with non-conservative forces.

A.1 Lagrangian

By substituting the expressions for the displacements of the centers of mass, as given in Eq. 1, into the the kinetic and potential energy expressions, Eq. 11 and Eq. 12, respectively, the Lagrangian can be expressed as follows:

$$\begin{aligned} L = & \frac{1}{2} m_1 \left(\dot{u}_1 + \dot{x}_G\right)^2 + \frac{1}{2} m_1 \dot{v}_1^2 + \frac{1}{2} J_1 \dot{\phi_1}^2 \\ & + \frac{1}{2} m_2 \left(\dot{u}_2 + \dot{x}_G\right)^2 + \frac{1}{2} m_2 \dot{v}_1^2 + \frac{1}{2} J_2 \dot{\phi_1}^2 \\ & + \frac{1}{2} m_c \left(\dot{u}_2 - \dot{\phi}_1 y_c + \dot{x}_G\right)^2 + \frac{1}{2} m_c \left(\dot{v}_1 + \dot{\phi}_1 x_c\right)^2 \\ & + \frac{1}{2} M_h \left(\dot{u}_h + \dot{x}_G\right)^2 + \frac{1}{2} M_I \dot{u}_h^2 + \\ & - m_1 g v_1 - m_2 g v_1 - m_c g \left(v_1 + \phi_1 x_c\right). \end{aligned} \tag{23}$$

A.2 Non-conservative virtual work

The various contributions to the virtual work of non-conservative forces, as reported in Eq. 14, are evaluated in detail below.

The virtual work contributions defined in Eq. 14 can be expressed as follows:

$$\begin{aligned} \delta W_{is} &= \left(2F_{is}^- - 2F_{is}^+\right) \delta u_1 + \left(2F_{is}^+ - 2F_{is}^-\right) \delta u_2, \\ \delta W_h &= -F_h \delta u_2 - F_h l_y^* \delta \phi_1 + F_h \delta u_h, \\ \delta W_s &= F_{sv} \delta v_1 + F_{su} \delta u_1 + C_s \delta \phi_1, \end{aligned} \tag{24}$$

In the last expression, the following terms are introduced to highlight the distinct contributions depending on both displacements

and velocities, grouped according to the corresponding generalized forces:

$$\begin{aligned} F_{su} &:= -2l_y\left(k_s u_1 + c_s \dot{u}_1\right), \\ F_{sv} &:= -2l_x\left(k_s v_1 + c_s \dot{v}_1\right), \\ C_s &:= -\frac{2}{3}\left(l_x^3 + l_y^3\right)\left(k_s \phi_1 + c_s \dot{\phi}_1\right). \end{aligned} \tag{25}$$

Thus, from the total virtual work, $\delta W = \mathbf{Q}^T \delta \mathbf{q}$, the vector of the generalized forces follows:

$$\mathbf{Q} = \left(2F_{is}^- - 2F_{is}^+ + F_{su} \;\; F_{sv} \;\; C_s - F_h l_y^* \;\; 2F_{is}^+ - 2F_{is}^- - F_h \;\; F_h\right)^T. \tag{26}$$

A.3 Equations of motion

Finally, substituting Eqs. 23, 24, 2, 25 and Eq. 26 in Eq. 15, the equations of motion, as presented in Eq. 16, are obtained.

B Equations of Motion of the non-isolated System

This section presents the equations of motion for the non-isolated system, i.e., without internal frames and control devices. These equations are derived using the Lagrangian formulation based on a reduced set of degrees of freedom (u_1, v_1, ϕ_1), along with the evaluation of virtual work associated with the non-conservative forces provided solely by the soil. Omitting the details, the resulting equations are:

$$\begin{aligned} &\left(m_1 + m_c\right)\ddot{u}_1 - m_c y_c \ddot{\phi}_1 + 2k_s l_y u_1 + 2c_s l_y \dot{u}_1 \\ &= -\left(m_1 + m_c\right)\ddot{x}_G, \\ &\left(m_1 + m_c\right)\ddot{v}_1 + m_c x_c \ddot{\phi}_1 + 2k_s l_x v_1 + 2c_s l_x \dot{v}_1 \\ &= -\left(m_1 + m_c\right) g, \\ &\left[J_1 + m_c\left(x_c^2 + y_c^2\right)\right]\ddot{\phi}_1 + m_c\left(x_c \ddot{v}_1 - y_c \ddot{u}_1\right) \\ &+ \frac{2}{3}k_s\left(l_x^3 + l_y^3\right)\phi_1 + \frac{2}{3}c_s\left(l_x^3 + l_y^3\right)\dot{\phi}_1 \\ &= m_c y_c \ddot{x}_G - m_c x_c g. \end{aligned} \tag{27}$$